The Design of a Gamma-Ray Tomographic Sensor for Detecting Mushy Zone in Continuous Casting

by

DongSik Kim

S.B., Mechanical Engineering, HanYang University (1994)

Submitted to the Department of Mechanical Engineering
in Partial Fulfillment of the Requirements for the Degree of

MASTER OF SCIENCE IN MECHANICAL ENGINEERING

at the

MASSACHUSETTS INSTITUTE OF TECHNOLOGY

June 1996

Signature of Author: _____
Department of Mechanical Engineering
May 31, 1996

Certified by: _____
Jung-Hoon Chun
Edgerton Associate Professor of Mechanical Engineering
Thesis Supervisor

Certified by: _____
Nannaji Saka
Principal Research Scientist, Mechanical Engineering
isor

Accepted by: _____
Ain A. Sonin
Professor of Mechanical Engineering
Chairman, Department Graduate Committee

The Design of a Gamma-Ray Tomographic Sensor for Detecting Mushy Zone in Continuous Casting

by

DongSik Kim

Submitted to the Department of Mechanical Engineering
on May 31, 1996 in Partial Fulfillment of the Requirements for the Degree of
Master of Science in Mechanical Engineering

ABSTRACT

The γ-ray tomographic sensor invented by the CastScan consortium at MIT for the non-invasive real time monitoring of the solidification front in the continuous casting of metals is a new industrial computed tomography (CT) tool. The sensor potentially offers great economic benefits to the continuous casting industry by preventing break-outs, and increasing productivity and efficiency through optimal process control.

In this thesis, the proposed concept was experimentally verified, based on radiation attenuation measurements, to prove its viability for determining the thicknesses of the liquid and solid sections of a solidifying metal, with a density difference as low as 7%. In addition, the preliminary experiments identified several fundamental factors that affect the operation of the sensor and which must be considered in the prototype design.

The γ-ray sensor integrates numerous system components: the radiation source, detector array, actuators, and tomographic algorithms. Therefore, in developing an effective sensor that meets various industrial specifications, component design and system integration must be optimized.

A CT sensor was designed specifically for detecting the mushy zone in continuous casting. Through mathematical modeling of radiation attenuation through the liquid and solid phases, quantitative relationships among source strength, exposure time, and other critical system parameters were established. These relationships serve as a quantitative framework for the design of an industrial tomographic system. In addition, optimal spatial resolution and tomography techniques for identifying the mushy zone were investigated and confirmed by simulations using several critical parameters, such as the number of translational and angular steps. From these considerations, the approach of generating 3D tomographic image of density profile across the liquid-solid interface from radiation attenuation data offers a superior and more direct method than the conventional approaches.

In conclusion, the tomography system geared to mushy zone identification can serve as a standard model for the CT sensor. Furthermore, the guidelines developed in this thesis can be used to design the future generations of sensors for different applications.

Thesis Advisor: Jung-Hoon Chun
Title: Esther and Harold E. Edgerton Associate Professor of Mechanical Engineering

Thesis Advisor: Nannaji Saka
Title: Principal Research Scientist, Mechanical Engineering

Acknowledgments

It seems like yesterday that I dared to expand my career horizons at an American university, far from my home in Korea. Today, I find myself on the verge of graduation with a Master's degree. Without the generous support of many wonderful people I would not have been able to reach this goal. First and foremost, my appreciation goes to Professor Jung-Hoon Chun who not only gave me the opportunity to work on the CastScan project, but also provided me with invaluable support and guidance from the time I arrived at MIT in 1994. I would like to thank him for helping me navigate through the complexities of a new culture and through the academic regimen of MIT. A special appreciation also goes to Dr. Nannaji Saka for his commitment and academic guidance, and especially for encouraging me to finish my thesis this semester. I would also like to thank Dr. Richard Lanza for teaching me a new area of tomographic technology.

Also, my thanks go out to various MIT faculty and staff for their kind assistance including Jeff DiTullio, Fred Cote, Gerry Wentworth, Julie Drennan, Leslie Regan, Joan Kravit, and Leanna Harada.

I especially want to thank the students at the Laboratory for Manufacturing and Productivity for sharing their knowledge and ideas with me: Sukyoung Chey, Jeanie Cherng, Ho-Young Kim and Chen-An Chen. In particular, I would like to thank Pyongwon Yim for mentoring and helping me solve various problems. I would also like to thank Imad Jureidini, my labmate, for being "so nice" to me while sailing on the same ship, and Mark Hytros, my partner in crime on this project — I will always remember the outrageous fun we had in California.

All of my friends in the Korean Graduate Student Association, including Sooyung Lee and Henry Choi, have provided me with invaluable technical support for which I am truly grateful. Without all the information they shared with me, I would not have been able to make any progress.

I am deeply indebted to all of my professors at Hanyang University in Korea, especially to Professors Jangkeun Yim, Joosung Meang, Kyungjin Park, Wooseung Kim, Changsoo Han and Sungkyu Ha. My gratitude also goes to the SOME (Study Of Mechanical Engineering) fellows including Jangwook, Sungwook, Hyunjun, Jongsoo and Jaeheon, whose support and trust in me carried me through some grueling times at MIT.

Finally, my family deserves much gratitude for their love, trust, warm care, and generous support throughout my life. I especially thank my sister, Jungyeoun, for being patient with me while I worked toward this degree.

Table of Contents

List of Tables

List of Figures

CHAPTER 1

INTRODUCTION

1.1 Background

In aluminum and steel industries, commercial size ingots/strands are commonly cast by continuous casting or by direct-chill casting process. In both processes, there is always a solidification front, i.e., a liquid-solid interface. The position and shape of the interface strongly depend on the heat flow rate out of the mold, the secondary cooling system, and the rate at which the strand is drawn from the caster. The shape and stability of the solidification front determine the casting rate and product quality. The velocity of the liquid/solid interface determines the microstructure and properties of the cast material. Thus, real-time tracking of the solidification front has a significant positive economic impact.

In the continuous casting process, the casting speed, i.e., the production rate, is largely limited by the strength of the solidified shell and by the location of the tip of the solidification front since partially solidified strands are continuously withdrawn through casters. Thus, a knowledge of the detailed shape of the liquid/solid interface on a continuous basis permits the operator not only to increase the casting speed by as much as 10 %, but to avoid break-out accidents. A typical steel casting plant has one break-out accident per month, which costs about $250,000 due to clean-up and lost production. While the economic significance demands a better sensor technology, at present there are no on-line sensors for monitoring the shape and position of the solidification front.

A new method for on-line measurement of solidification front for casting of aluminum alloys was developed by MIT. The proposed method uses high energy (5 to 10 MeV) γ-rays generated by a compact, electron linear accelerator (LINAC) to measure the differences in γ-ray transmissivity due to the density differences, typically 4 - 12 % higher for the solid compared with that of the liquid metals (Chun et al., 1995). The γ-ray sensor being developed at MIT integrates many components, such as a radiation source, detector, actuator, and tomographic device. In this integration effort, there are many variables for each components, such as source strength, actuation method, and detector type. Factors that determine the final configuration of the sensor include: spatial resolution, image contrast, signal-to-noise ratio, measurement time, and caster size. These factors

have a primary influence on the performance and cost of the sensor, as well as the method. Therefore, a working relationship between these controlling factors should be developed.

The solidification process of an alloy is characterized by the existence of a mushy zone, in which the solid and liquid phases coexist and it has a crucial role on the quality of metal product and the production rate. In this sense, the study of the mushy zone has well founded. To be sure, characterizing of the mushy zone may not be necessary just for monitoring the solidification front in continuous casting. However, characterizing the mushy zone should guarantee a satisfactory performance requirements. For this reason, mushy zone characterization is the upper bound goal.

Therefore, if a γ-ray tomographic system is designed for detecting the mushy zone, it should serve as a standard model of the proposed sensor. Especially, for the first industrial application of the proposed sensor technology in a large caster, an actual aluminum foundry settings will be used as a prototype. Through this design process, as with every process following it, it is believed that the system configuration solution for future generations of this sensor in different plants and applications can be achieved.

1.2 Scope of Research

This thesis is divided into two main parts. The first part is the feasibility study, by several preliminary experiments, to test the viability of the proposed concept. In particular, the application of computed tomography (CT) for the identification of density variations is tested and the problems are analyzed. The second part comprises the design process. Criteria of the design and characteristics of the high energy CT application are addressed before the actual design. The component design and some useful computer tomographic techniques are also conducted. The goals of this thesis are:

- Feasibility study of the CT system to detect the liquid/solid interface in metal solidification process,
- Identification and characterization of the critical parameters of the CT system,
- Investigation of the optimal spatial resolution to accurately identify critical solidification front characteristics, including mushy zone identification,
- Evaluation of the various tomographic techniques and trade-offs for optimal real-time monitoring of the solidification front,
- Development of the design criteria for industrial-scale application, and

- Design of the each components to meet the specification and integration of components for the optimal performance.

1.3 Outline

This chapter provides background and scope of the project. In Chapter 2, description of the solidification process anda brief review of the mushy zone research are presented. Chapter 3 gives the proposed concept of developing an on-line tomographic sensor for monitoring the solidification process. In addition, viability of the Computed Tomographic sensor is verified by the feasibility study by a set of preliminary experiments. In Chapter 4, prior to the design process, all the information are documented including the primary design characteristics and design criteria of the each components for high energy CT system and the fundamental issues which have to be considered in this application . Finally, Chapter 5 describes some useful design approaches, which need to be conducted in preparation for an actual industrial setting.

CHAPTER 2

CONTINUOUS CASTING PROCESS AND MUSHY ZONE

2.1 Continuous Casting Process

Continuous casting is entering a new era of development, not only with respect to its increasing application in the production process, but also in its own evolution as a process and its interaction with other processes in metal manufacture. Continuous casting output has shown an accelerating growth. It is responsible for more than 50 % of current steel production in the world, and more than 80% in Japan. The principal advantages of continuous casting are a substantial increase in yield, a more uniform product, energy savings, higher manpower productivity, and reduced pollution. These advantages and the ease of integration into metal production systems have led to a wide application of the continuous casting process.

2.1.1 General process description

The purpose of continuous casting is to bypass conventional ingot casting and to cast to a form that can be directly rollable on finishing mills. The use of this process results in the improvement in yield, surface condition, and internal quality of product when compared with ingot-made material (Pehlke, 1992).

The sequence of operations of continuous casting is as follows:

- Delivery of liquid metal to the casting strand,
- Flow of metal through a tundish into the casting mold,
- Formation of the cast section in a water-cooled copper mold,
- Continuous withdrawal of the casting from the mold,
- Further heat removal to solidify the liquid core by water spraying beyond the mold, and
- Cutting to length and removing the cast sections.

Schematic of a continuous casting machine is depicted in Figure 2.1. Molten metal in a ladle is delivered to a reservoir above the continuous casting machine called a tundish.

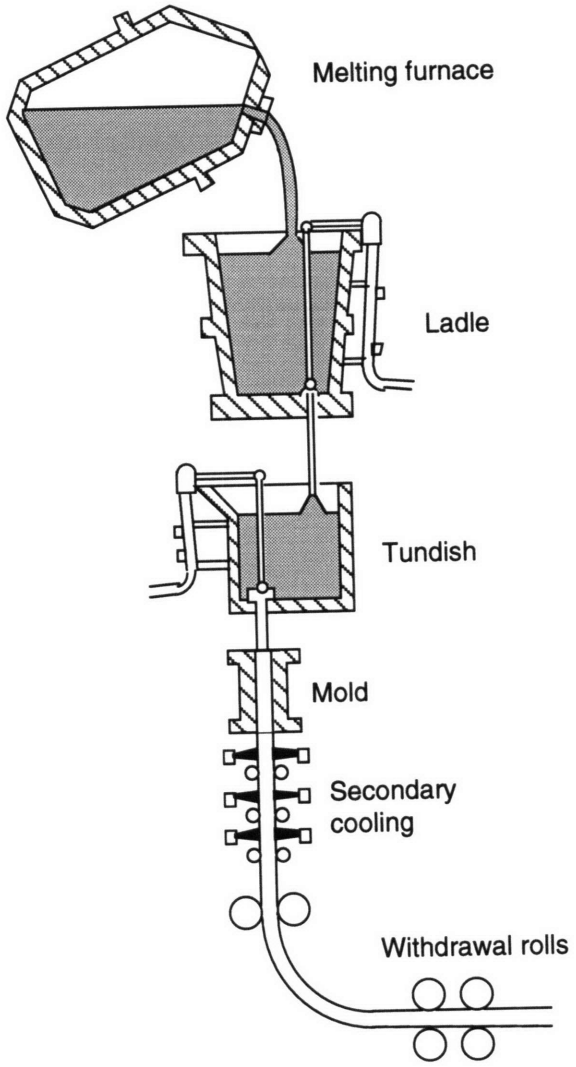

Figure 2.1 Schematic of continuous caster.

The metal from the tundish flows into one or more open-ended, water-cooled copper molds which are controlled by a stopper rod-nozzle or slide gate valve arrangement. A dummy bar, i.e., a starter, is inserted into the mold in order to initiate a cast, and sealed to contain the initial flow of metal in the mold and to form a solid skin. After the mold has been filled to the desired height, the dummy bar is gradually withdrawn at the same rate that molten metal is added to the mold. The initial liquid metal solidifies onto a suitable attachment of the dummy bar so that the cast strand can be withdrawn down. Solidification of a shell begins immediately at the surface of the copper mold. The length of the mold and the casting speed are adjusted such that the shell thickness is capable of withstanding the pressures of the molten metal core on exiting from the copper mold. Generally, the mold is

oscillated and a lubricant is added to the mold during the casting operation to avoid sticking of the frozen shell to the copper mold. The rolls below the mold, where the secondary cooling is performed by spraying cooling water onto the strand surface to complete the solidification process, support the metal strand mechanically. After this process, the fully solidified strand is sectioned into desired lengths by a cut-off torch or shear. This final portion of the continuous casting machine also has provision for disengagement and storage of the dummy bar.

There are many types of continuous casting machines in use such as vertical, vertical with bending, curved or S-strand with either straight or curved mold, curved strand with continuous bending, and horizontal. Most of the original continuous casting machines for steel were vertical machines. Although more complicated in their construction, vertical machines with bending and curved strand machines were developed to minimize the height of the machine and allow installation in existing plants without modification of crane height.

2.1.2 Future developments

The emphasis on the further development of continuous casting will focus on monitoring and controlling the solidification process, with the objective of maintaining high quality and high productivity since the solidification process influences the final properties of the product and limits the product rate at which a solidifying strand can be extracted from a continuous caster. Accomplishing this includes monitoring metal quality and ensuring that all aspects of the process are under the proper control. Especially, when the extraction velocity is too high, the partially solidified shell will rapture, resulting in a "break-out" accident, whereby molten metal spills from the strand and the tundish into the work place. Break-out accident costs tremendously because production shutdown is required during the clean-up period. Therefore, developing a sensor to avoid the possibility of the break-out is strongly required.

2.2 Mushy Zone Research

Solidification of alloys is characterized by the existence of a mushy zone, in which the solid and liquid phases coexist (Flemings, 1974). It has been reported that transport phenomena (i.e., heat, mass transfer and fluid flow) in the mushy zone are the major cause

for the formation of casting defects such as segregation, porosity and hot tears (Flemings, 1974; Fisher 1981). In particular, the formation of macrosegregation (i.e., a large-scale non-uniformity in composition) in castings is caused by two processes occurring in the mushy zone during solidification (Flemings, 1974). The first corresponds to the floating or settling of solidified phases. The solidified phases could be equiaxed grains and/or broken dendrites in the mushy zone. The second mechanism is related to the flow of solute-rich or solute-poor liquid in the mushy zone. The fluid flow, in turn, can be caused by shrinkage and or thermal and/or solute gradients. A higher concentration of solute is found near the bottom surface of the casting in the unidirectionally solidified casting, which is called inverse segregation. It is a kind of macrosegregation caused by solidification contraction.

Many experimental and theoretical studies have been conducted on the segregation phenomenon (Scheil, 1947; Kirkaldy and Youdelis, 1958) to understand the mechanics of the mushy zone. The first rigorous model to predict the formation of macrosegregation was by Flemings (1974). The well-known "local solute redistribution" equation successfully predicts the formation of inverse segregation, centerline segregation, and the changes resulting from varying the cross-section of a mold. The solute diffusion, however, was neglected, and the thermal gradients and velocity distributions used in the analysis were either measured or assumed.

In the unidirectional solidification of Al-Cu alloys cooled from the bottom, the heavier copper species is rejected when the solid aluminum is precipitated, stable solute and temperature gradients are created, and no natural convection can be induced. Hence, the inverse segregation in the directionally solidified Al-Cu alloys cannot be predicted by the earlier models. It has been concluded that shrinkage-induced flow is dominant in the mushy zone compared with the natural convection due to temperature gradients (Chiang and Tsai 1992).

A key element of mushy zone modeling is the description of the microscopic evolution of the length-scales within the mushy zone and the influence of macroscopic transport processes. Glicksman et al. (1992, 1994) summarized some recent progress in the development of a mean-field statistical theory of phase coarsening in adiabatic mushy zones. Theoretical outcomes of their work were the development of temporal scaling laws for the length scales and determination of coarsening dependencies on material parameters and solid volume fraction. High precision thermal decay experiments have verified some aspects of the theory for mushy zones held under adiabatic conditions and integrating the microscopic coarsening theory within a simple macroscopic heat-transfer model of one-

dimensional alloy solidification demonstrated the influence of macroscopic heat transfer on the evolution of primary and secondary dendrite arm spacing in the Al-Cu alloys.

Diao and Tsai (1994) have developed a mathematical model to predict the formulation of macrosegregation for the unidirectional solidification of Al-Cu alloys. The model based on the continuum formulation allowed the calculation of transient distributions of temperature, velocity, and species in the solidifying alloy caused by thermo-solutal convection and shrinkage-induced fluid flow. It was found that two mechanisms in the mushy zone, i.e., the floating or settling of precipitated phases during the solidification process and the flow of either solute-rich or solute-poor liquid into the mushy zone contribute to macrosegregation. By comparing with experimental data, they proved that their model could accurately predict the formation of inverse segregation.

From the brief literature survey, it is apparent that the microstructure of castings greatly depends on what happens in the mushy zone. Solidification defects such as porosity, micro- and macrosegregation, clearly depend on the heat and mass transfer and fluid flow in the mushy zone. These transport processes, in turn, depend on the shape, size and velocity of the liquid/solid interface in continuous casting. Hence, the need for characterizing the mushy zone can not be overstated.

CHAPTER 3

THE PROPOSED CONCEPT AND PRELIMINARY EXPERIMENTS

3.1 The Proposed Concept

The sensor method is based on the attenuation of high-energy γ-ray photons through the solidifying strand as well as through any surrounding ancillary equipment. Possible radiation sources include radioisotopes, such as Co^{60} and a compact, electron linear accelerators (LINAC), which are commercially available and produce a continuous energy spectrum up to 10 MeV. At these high energies, the attenuation of most metals is dominated by Compton scattering and is essentially independent of material type, instead determined almost completely by the density of the material (Evans, 1955). This is shown in Figure 3.1, in which the total cross-sections versus energy are plotted for aluminum and iron. Above 4 MeV, the curves flatten out, indicating the lack of energy dependence. The strength of the required radiation source, however, depends on the thickness and density of the strand being cast.

An on-line measurement technique for determining the shape and location of the solidification front is schematically presented in Figure 3.2 (Chun et al., 1995). Radiation from the source S is collimated to produce a narrow beam. The beam exits the aperture of the collimator and traverses the path S1234D from the source to the detector array D. Along this path, the γ-ray beam travels through air, the solidified metal (path 1-2), the liquid metal (path 2-3), the solidified metal again (path 3-4), and finally through air to the detector. During its travel, the photon beam is attenuated mostly by the solid and liquid metals, thus the detected beam intensity is less than the incident beam intensity. The mass attenuation coefficients of liquid and solid metal are the same, but their densities differ by about 6 % for steel and 12 % for aluminum. As a result, it is possible to calculate the path lengths of the beam through the liquid and solid phases in the strand.

By rotating and translating the source-detector array about the longitudinal axis of the solidifying strand, a complete profile of the solidification front can be mapped. A tomographic image providing a full three-dimensional solidification profile, including mushy zone density distribution within the strand, can thus be constructed using reconstruction techniques similar to those of computerized tomography used in medical imaging.

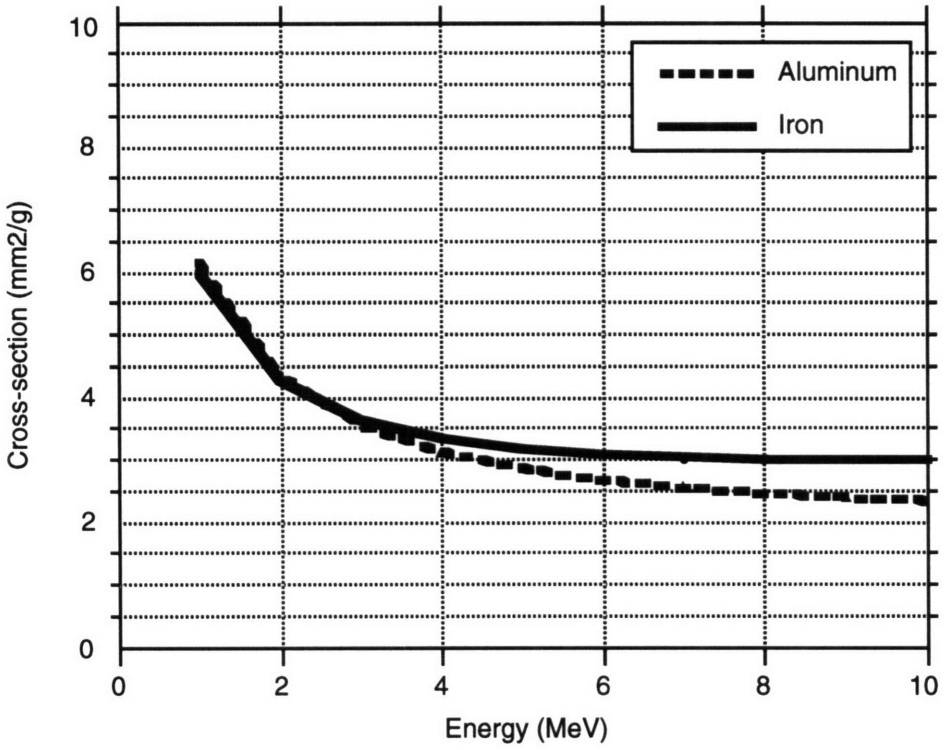

Figure 3.1 Attenuation coefficient versus energy.

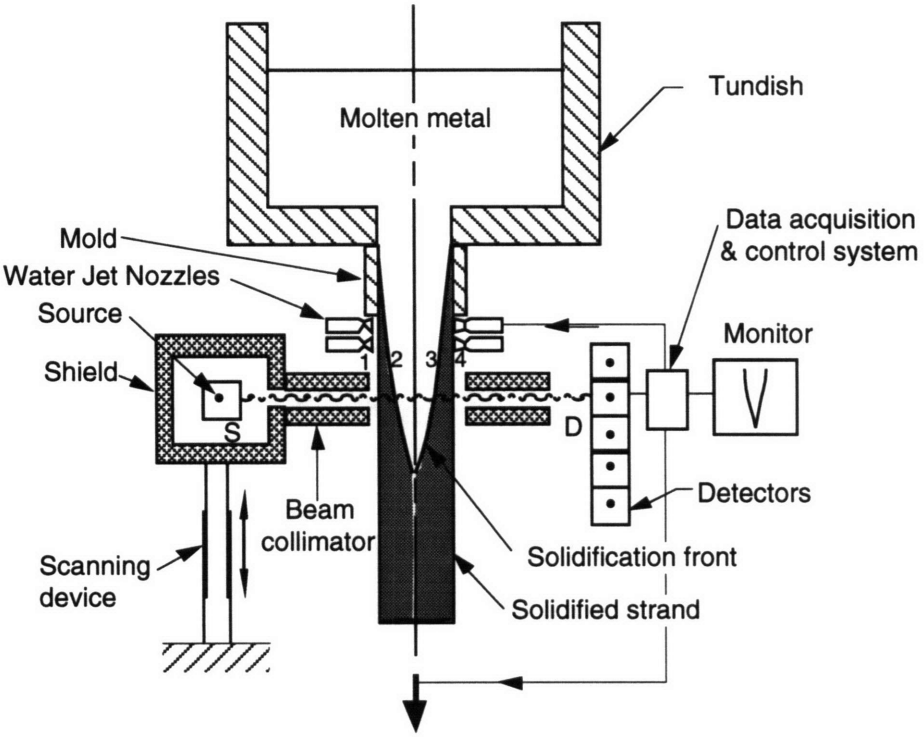

Figure 3.2 Schematic of the proposed technique for detecting solidification front.

The advantages of the proposed technique are obvious. First, this novel technique is non-invasive. Second, the speed of detection is relatively fast. Third, the composition of the liquid metal need not be changed for detecting the liquid/solid interface. Finally, the cast ingot need not be sectioned and prepared for metallographic examination for extracting information regarding the profile of the liquid/solid interface. These features make the proposed technique feasible for on-line measurement and control of the continuous casting operation.

3.2 Theoretical and Practical Considerations

Using the exponential attenuation relation, the number of γ-ray photons, N, transmitted through the strand in a given time may be written as:

$$N = N_o \exp\left\{-\left(\mu\rho_s x_s + \mu\rho_l x_l\right)\right\} + fN_o \ ,$$

or

$$N = N_o \exp\left\{-\left[\mu\rho_s\left(L - x_l\right) + \mu\rho_l x_l\right]\right\} + fN_o \ , \tag{3.1}$$

where N is the number of photons transmitted through the material subject to the radiation, N_o is the number of photons incident, μ is the mass attenuation coefficient, ρ_s is the density of the solid, ρ_l is the density of the liquid, L is the total path length through the strand (path 1-4), x_s and x_l are the path lengths through the solid and liquid portion, and f is the fraction of the incident radiation that is forward scattered. Neglecting forward scattering, equation (3.1) can be rewritten as:

$$\ln\left(\frac{N}{N_o}\right) = \mu\left(\rho_s - \rho_l\right)x_l - \mu\rho_s L \ . \tag{3.2}$$

Thus, if scattering is not explicitly accounted for, i.e., if equation (3.2) is used instead of the more accurate equation (3.1), the increased number of detected γ-rays due to forward scattering, the second term (fN_o) in equation (3.1) will be ascribed to a reduced amount of attenuation and hence a smaller value for the mass absorption coefficient will be obtained. This effect will be most pronounced for thick absorbers where scattering will be the largest. By a combination of energy selection and collimation of the beam at the

detector, the scattered radiation can be reduced considerably. However, in the case of a continuous energy spectrum, only collimation can be used.

The mass attenuation coefficient, μ, is independent of the density and physical state of the material. It varies only as a function of the incident photon energy. Furthermore, since it is nearly constant in the range of the photon energy we use, as shown in Figure 3.1, rendering the ratio of the number of photons surviving through the material to the number of incident photons can be accomplished, Thus a simple and unambiguous exponential decay function of the distance, the distance of liquid and solid portion, can be readily calculated.

3.3 Apparatus

3.3.1 Source and detector

Among many gamma radiation sources, the Co^{60} radioisotope was used for the gamma radiation in the preliminary experiments. The source strength was 7 mCi and it produced the gamma photons at two distinct energies, 1.17 MeV and 1.33 MeV. The radioisotope was shielded in a cylindrical lead housing with a 6 mm diameter hole drilled through its side. This housing served as a pencil-beam type aperture and collimator for the gamma photons.

A single $100 \times 100 \times 100$ mm Rexon Technologies model NAI4-4MX4-3 sodium-iodide (NaI) scintillation detector was used to collect the gamma photons. The output of the detector was amplified by a Canberra model 1412 research amplifier and connected to a Canberra model 2037A edge/crossover timing counter. The detector was filled with a collimator of 2 mm diameter aperture size.

3.3.2 Data acquisition and control system

Since the photon flux from the Co^{60} source is relatively low, the photon count measurements were performed in a pulse mode. The photon count measurement program was written in C language. The signal output from the Canberra edge-crossover timing counter was connected to a Keithly-Metrabyte DAS-1601 analog-digital input-output board with a 12-bit resolution. The photon count was measured over a chosen count time and

incorporated in the data acquisition program. The test-object was moved relative to the γ-ray source and detector.

The positioning stage comprised a motorized rotary table mounted on a motorized horizontal translation table, which in turn was mounted on a manual vertical translation table. The rotary table was a New England Affiliated Technologies RT-4-SM model with a 99 mm diameter platform. The minimum angular step size was 0.02 degree, with an accuracy of 180 seconds and a repeatability of 36 seconds. The horizontal translation table was a New England Affiliated Technologies TM-800-SM model with a travel span of 203 mm. The horizontal translation table had a resolution of 0.01 mm. These rotary and horizontal table were driven by a 5 volt, 0.353 N-m (50 oz-inch) stepper motor operating at 200 steps per revolution.

The vertical translation table was a Newport model 281 laboratory jack with a range of 76 mm and 3 mrad parallelism. Positioning was performed manually by turning the lead screw. The positioning stage was leveled and mounted so that the test object could be moved perpendicular to the path of the γ-ray beam. The positioning stage control system comprised a NuLogic 2-axis NuDrive stepper motor amplifier and a NuLogic PCStep motion control board. The two stepper motors driving the rotary and horizontal positioning tables were connected to the amplifier and operated with the motor controller card. An open-loop control scheme was used. The appropriate motor was incremented by this amount at a preset velocity and acceleration. The system allowed the positioning stage to be moved in well-defined increments with respect to a fixed origin.

3.3.3 Reconstruction program and image display

Two-dimensional tomographic images of the test object were reconstructed using a Filtered Back Projection (FBP) algorithm in FORTRAN. The tomographic images were displayed and analyzed using a Matlab matrix manipulation software package. Both programs were executed on a Sun Sparcstation 5 computer with a UNIX operating system. The reconstruction program allowed the user to specify the cut-off frequency and the mathematical order of one of five filters (ramp, Hamming, Hann, Parzen, or Butterworth) for the FBP algorithm.

3.3.4 Temperature measurement

Since temperature measurements were required to locate the position of the solidification front, data acquisition was performed using Omega chromel-alumel (K-type) thermocouples in conjunction with a Keithly-Metrabyte DAS-TC data temperature measurement board. The software supplied with the DAS-TC board was used to record the temperatures, which were measured over the same time interval as the photon count and recorded in conjunction with a control program. The thermocouples had a diameter of 1.6 mm and a length of 203 mm. The thermocouple accuracy was 2.2 °C and the DAS-TC board accuracy was 0.05 °C.

3.4 System Calibration

The system was calibrated by measuring the γ-ray attenuation through various known thicknesses of solid tin. The photon count was measured for beam attenuation though 10, 20, and 30 mm of tin with no collimator. Four trial experiments were performed and five samples were recorded, each over a 10 second interval, and averaged for each experiment. Results of this calibration experiment are shown in Figure 3.3.

The linear relationship between the natural logarithm of the normalized γ-ray counts and the thickness of solid tin agrees well with equation (3.2). Using the calibration data and equation (3.3) below, the mass attenuation coefficient was calculated to be 0.00445 m^2/kg.

$$\mu_{exp} = \frac{\ln(I_o/I)}{\rho x_{tin}} \tag{3.3}$$

This result was lower than the expected value of 0.00502 m^2/kg for tin at a mean Co^{60} energy of 1.25 MeV. This represents an error of 11.4 %. The lower than expected value for the mass attenuation coefficient is attributed to the detection of forward scattered radiation due to the use of an uncollimated detector. Since scattered radiation was present in the measurement, the measured photon count was higher than the normal transmitted photon count. If the value of I is higher than expected, the value of $\ln(I_o/I)$ is lower than expected, resulting in a lower value for the mass attenuation coefficient.

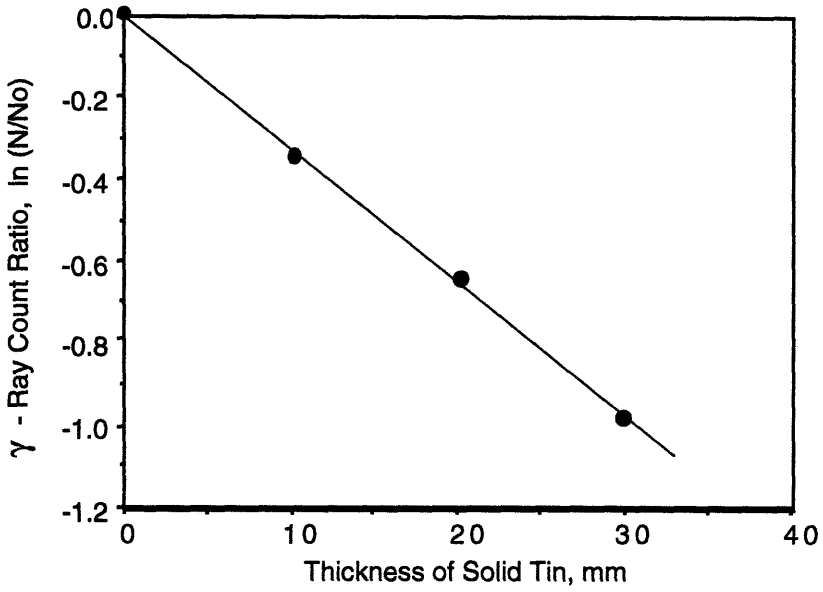

Figure 3.3 Calibration experiment.

3.5 Gamma-Ray Attenuation Experiments

An experimental setup for the γ-ray attenuation experiment, shown in Figure 3.4, was fabricated (Chun, 1995). A collimated beam (6 mm in diameter) of γ-rays from a Co^{60} source, mounted on a steel platform at a 45° angle relative to the horizontal, was directed to pass through a cylindrical graphite crucible (50.8 mm I.D.) filled with pure tin (2,570 mm^3). A NaI scintillation detector was also mounted at a 45° angle, in line with the photon beam. The crucible was heated at the top above its melting point by a band heater and cooled at the bottom by a water-cooled jacket. This selective heating and cooling allowed the tin to exist in the crucible in a steady two-phase state, i.e., as liquid and solid phases. Since the thermal conductivities of tin and graphite are relatively high, a stable, horizontal solidification profile was maintained. By varying the heating and cooling rates, the solidification front could be moved vertically. Thus, the γ-ray beam could encounter various path lengths in the liquid and solid phases of tin.

A tree of 8 chromel-alumel (K-type) thermocouples with a horizontal spacing of 28 mm and an inclination of 45° was installed inside the crucible to lie in-line with the γ-ray beam. The thermocouple-tree was used to monitor the temperature profile and thus to locate the position of the solidification front.

Ten sets of experiments were performed to determine the attenuation of the γ-ray beam by the graphite crucible, liquid tin, various proportions of liquid/solid tin, and solid

tin. Concurrently, the solidification front was tracked by the thermocouple-tree. For each experiment, the transmitted photon count was averaged over a series of 10 samples and a different solidification front position was set, altering the liquid/solid fraction along the beam path. For each solidification front position, the γ-ray counts were taken for 100 seconds. For solid and liquid tin, the counts were 7.84×10^4 and 8.36×10^4, respectively.

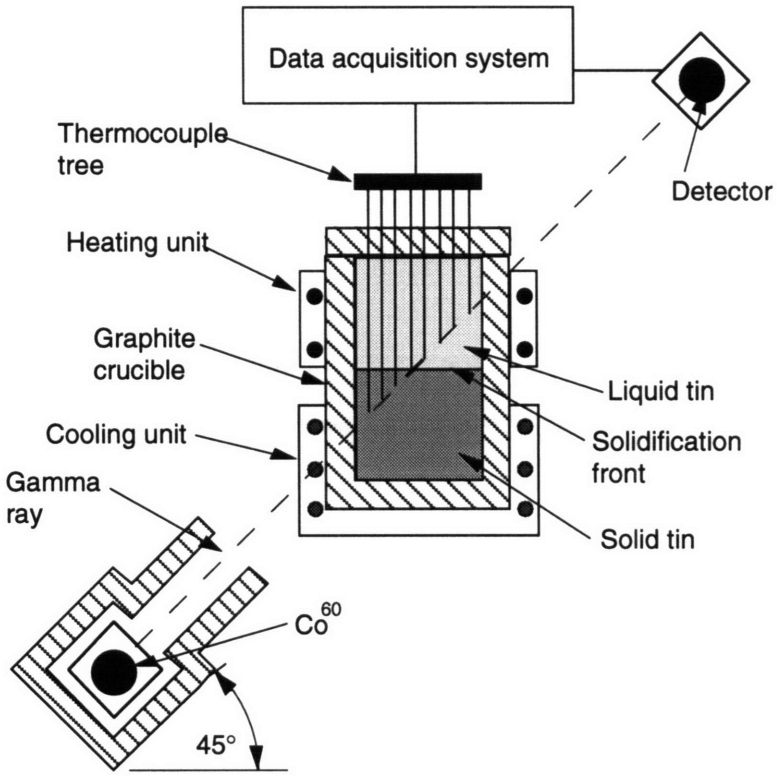

Figure 3.4 Experimental setup for γ-ray attenuation measurements.

The liquid path lengths were calculated by rewriting equation (3.2) as:

$$L_l = \frac{\ln(N/N_s)}{\mu(\rho_s - \rho_l)}, \tag{3.4}$$

where N_s is now the γ-ray photon count with solid tin in the crucible. Normalization by N_s rather than by N_o accounts for beam attenuation by the walls of the crucible, the heating/cooling system, solid tin, and the forward scattered beam.

Figure 3.5 plots the liquid path lengths calculated with $\rho_s - \rho_l$=300 kg/m^3 and μ= 0.00502 m^2/kg against those measured by the thermocouple method. Taking into

account the statistical error in the γ-ray count and the errors present in the system, including misalignments of the γ-ray beam with the thermocouple tree and the use of an uncollimated detector, it is apparent that the liquid path lengths estimated by the γ-ray attenuation method correlate well with those obtained by the thermocouple-tree technique. Consequently, the results provide the groundwork and motivation for further experiments of CT for determining the shape and location of the solidification front.

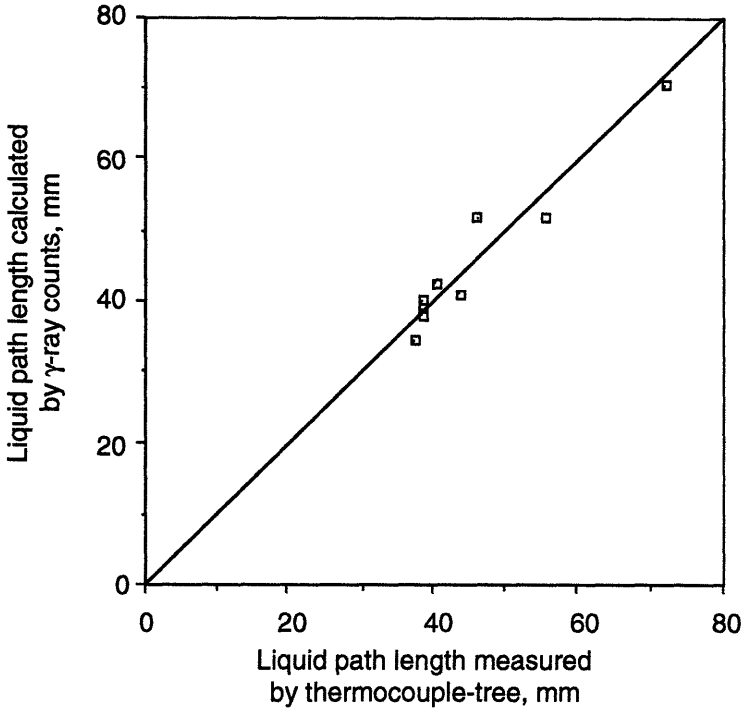

Figure 3.5 Comparison of liquid path length by γ-ray count and thermocouple measurements.

3.6 Tomographic Imaging Experiments

Several experiments increased understanding of the performance characteristics of a tomographic imaging system. Identical equipment was used to conduct all experiments, including a first generation actuator for movements and a FBP algorithm for reconstructing tomographic images from the projected data. A ramp filter with a cutoff frequency of 0.9 was used in all image reconstructions. This type of filter and high cutoff frequency provided the best edge detection and spatial resolution.

3.6.1 System performance evaluation

Preliminary experiments for the evaluation of the CT system were conducted (Hytros,1996). Of particular interest is an edge response test to determine the spatial and contrast resolution of a uniform aluminum block tomographic image. The aluminum block was 24 mm × 24 mm and 53 mm long. Four different source-to-object (STO) positions (118, 194, 292, and 367 mm) were used for the experiments regarding the spatial and contrast resolution capabilities of the CT system. For each scan, a single projection was recorded by moving the block across the beam at 0.25 mm increments over the 51 mm span. The photon attenuation at each of 200 translational positions were recorded with each measurement taken over a 240 second count time. The photon attenuation of a projection versus position for the four scans is shown in the Figure 3.6. The photon attenuation has been normalized as:

$$Pn(r,0) = \ln\left(\frac{I_o}{I}\right) = \rho\mu x \tag{3.5}$$

The theoretical response was also calculated by equation (3.5) with the known properties of the aluminum block, such as the density (ρ=2780 kg/m^3), the mass attenuation coefficient (μ=0.00550 m^2/kg), and the thickness (x=53.3 mm). The maximum value represents the normalized photon attenuation through the aluminum block, while the minimum value represents the normalized photon attenuation through air. In addition, the rise and fall of the slope were referred as the edge response. Figure 3.6 compares the results of the four experiments with the theoretical response across the aluminum block. The theoretical response is approximately 16 % greater than the largest maximum average response for the four scans. The primary source of this error is attributed to the detection of scattered radiation which made I greater, lowering normalized projection value and contrast resolution.

The spatial resolution of the system was calculated by analyzing the slope of the edge response. For the theoretical response, the spatial resolution is infinitely small which results in the rise of vertical edge response since an infinitesimal beam width was assumed. However, the rise of edge response has a finite slope for the photon beam with a finite width.

The contrast resolution, which will be discussed in detail in Section 4.6.2, is proportional to the linear attenuation coefficient. Photon attenuation through the aluminum block decreases as the STO distance increases, thus the linear attenuation coefficient of

aluminum also decreases. The decrease in the linear attenuation coefficient with a translational position is a direct result of the detection of a larger fraction of scattered radiation. The calculated results of the spatial resolution and contrast resolution are listed in Table 3.1.

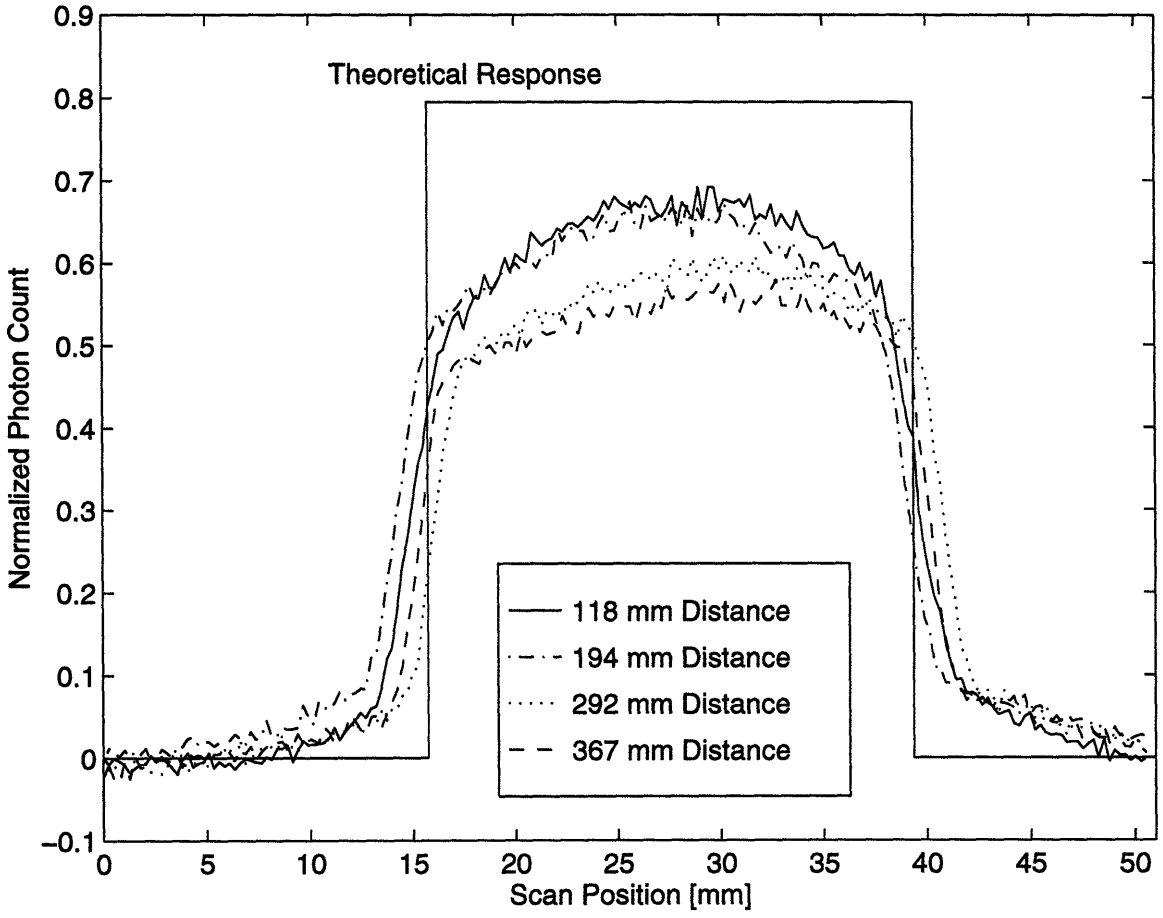

Figure 3.6 Comparison of the edge responses with theoretical prediction at various source-to-object distances.

Table 3.1 Results of the spatial resolution and contrast resolution.

Source-to-object distance (mm)	Average spatial resolution (mm)	Contrast resolution (%)
367	3.2	148,787
292	3.2	157,171
194	4.4	176,830
118	4.8	180,877

As determined by the edge response experiments, there is a trade-off between spatial resolution and contrast resolution of the CT system based on the STO position. The shorter STO distance produces better contrast resolution because of the lower amount of scattered radiation incident on the detector. However, the greater STO distance produces better spatial resolution.

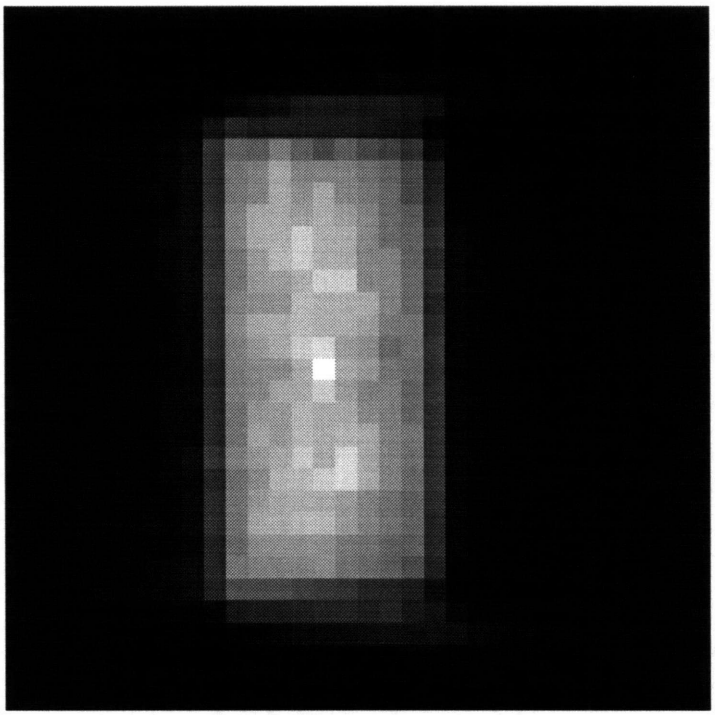

Figure 3.7 Reconstructed CT image of an aluminum block.

Figure 3.7 shows a tomographic image of the aluminum block, which was reconstructed based on the 194 mm STO distance, resulting in a reasonable trade-off between the spatial and contrast resolutions of the system. A step size of 2.4 mm for transverse measurements and 2.5° for the view angles were used. The photon count time for each measurement was 240 seconds, producing a photon count range within the data set of 10820 to 21884. The block geometry is defined by some blurring along the edge. The dimensions of the block image are roughly 9 to 11 steps by 20 to 24 steps, which translates into a size of 23.8±2.4 by 52.4±4.8 mm. This compares quite well with the actual block size of 24 × 53 mm, and the expected spatial resolution of 4.4 mm. This initial CT reconstruction of an aluminum block verifies the ability of the experimental system to adequately reproduce an object of a known size and shape. In addition, the reconstructed image has a spatial resolution comparable to the previous experimental analysis. The

system performance evaluation therefore proves the functionality of the CT system and provides the basis for further object imaging.

3.6.2 Aluminum cylinder experiments

Before testing a graphite crucible filled with two-phase tin, or an object with a complicated internal structure, a uniform cylindrical object was reconstructed in the second CT experiment. The diameter of the aluminum cylinder was 64 mm and the STO distance was 215 mm. A step size of 1.9 mm was used for the transverse measurements and 2.5° for the view angles, resulting in the total of 47 transverse steps and 72 view angles. The ratio of N_θ to N_s was 1.53, just under the minimum specified value of 1.57 for proper reconstruction. The photon count time for each measurements was 240 seconds which produced a photon count range within the data set of 9770 to 21958.

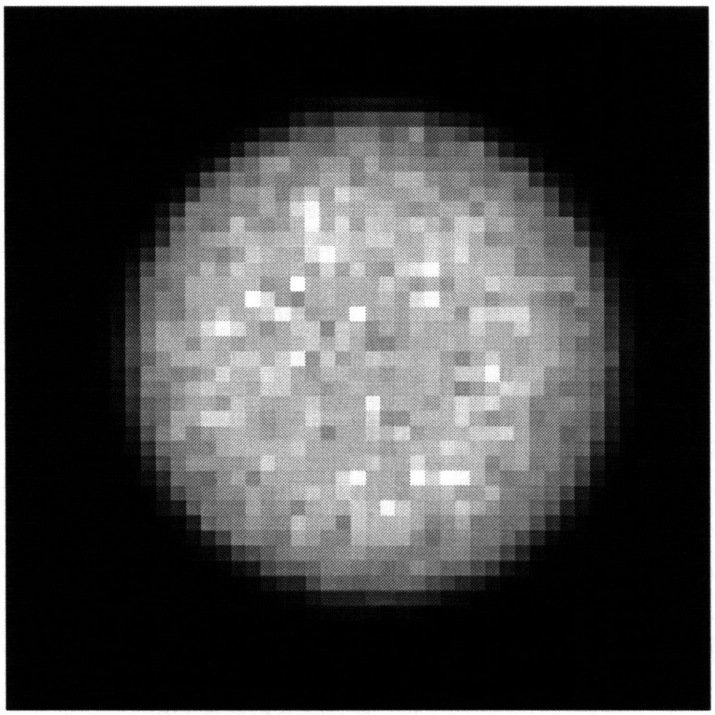

Figure 3.8 Reconstructed CT image of an aluminum cylinder.

Figure 3.8 shows the reconstructed image of the aluminum cylinder. The outside diameter of the cylinder is roughly 33 to 35 steps, which translates into a size of 64.8±1.9 mm, matching well the actual cylinder diameter of 64 mm. The contrast between air and the aluminum is very distinct, although the image is not completely uniform within

the aluminum cylinder because of variations, attributable to the statistical error from the photon count and noise in the image. This results implies that the experimental CT system operated properly with no discernible artifacts in the image and that the image size accurately matched the actual dimensions of the cylinder.

3.6.3 Tin cylinder in steel sleeve

The third experiment involved CT reconstruction of an object, which had a solid tin core surrounded by a steel ring. Since the density difference between solid tin and solid steel is approximately 6 to 7 %, the same as the density difference between liquid and solid steel, the geometry of this test object is ideal for simulating the solidification front as if it were being continuously cast. The tin represents the liquid core of the steel. Consequently, the object shown in Figure 3.9 (a) serves as a valuable test for detecting 6 to 7 % density difference and resolve a discrete interface.

The diameter of the tin cylinder was 38 mm and the outer diameter of the steel annulus was 64 mm. The STO distance was 215 mm and all the step sizes were identical to the parameters used in the experiments of the uniform aluminum cylinder. The photon count time was 300 seconds, which produced a photon count range within the data set of 7049 to 36471.

Figure 3.9 (b) shows the reconstructed image of the steel annulus and tin cylinder. The outer diameter of the steel annulus was estimated roughly 33 to 35 steps and the interior diameter was 18 to 20 steps which translates to 64.8±1.9 mm for outer diameter and 36.2±1.9 mm for interior diameter, respectively. Although the interface between the steel and tin is blurry, the image still compares very well with the actual geometry of the system. This result confirms that the system can accurately detect and image the density difference of 6 % with a good spatial and contrast resolution even though this object did not contain the molten portions. However, due to the weak photon flux from the Co^{60} source, the photon count time, i.e., the overall data acquisition time, had to be quite long to achieve good statistical data. This issue must be addressed in the design of the future system.

3.6.4 Two-phase metal experiment

The final experiment was to generate a CT image of the two-phase. It was set up as shown in Figure 3.10 and tested the feasibility of detecting the solidification front in a

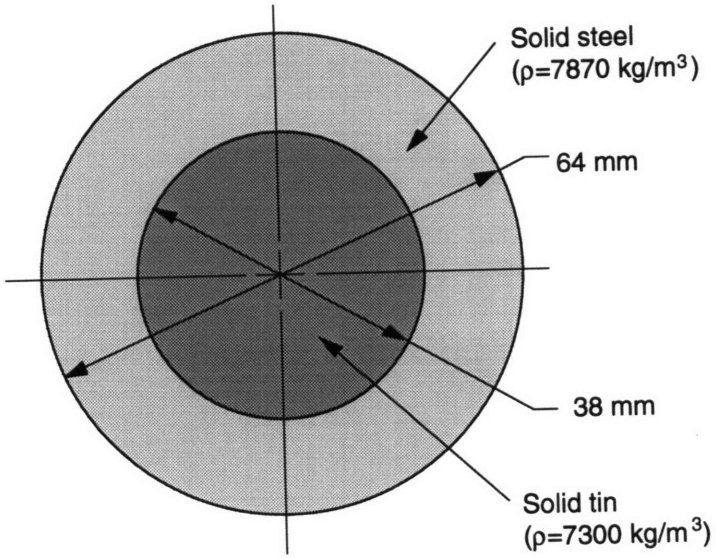

(a)

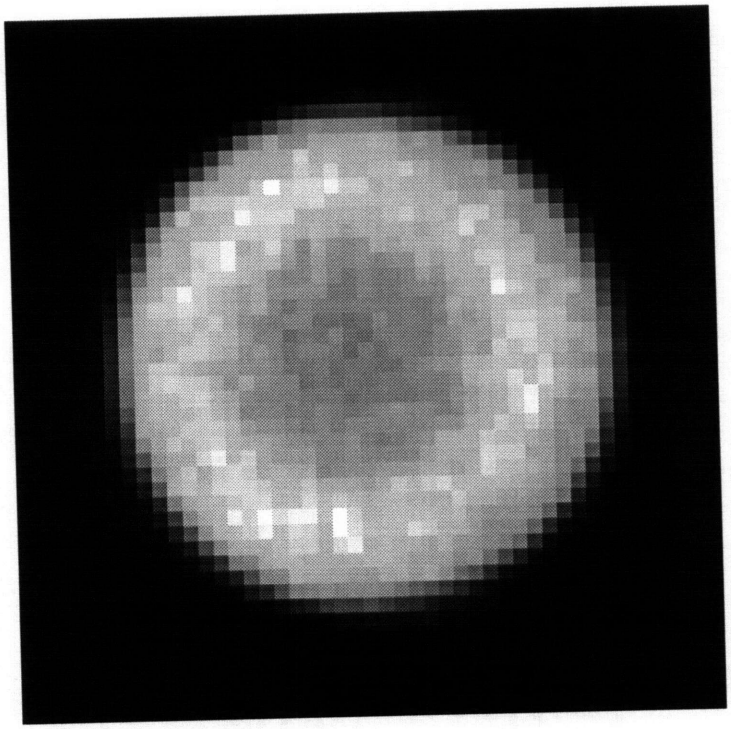

(b)

Figure 3.9 (a) Diagram of tin cylinder in steel sleeve, (b) Reconstructed CT image of a tin cylinder surrounded by a steel sleeve.

partially solidified casting. Pure tin was melted and poured into a graphite crucible. A cartridge heater enclosed in a copper sheath was mounted inside the crucible to melt a portion of the tin. After several heater positions were tested, an offset heater design was used for the final experiment. The crucible rested in a recess of a water-cooled aluminum chamber which solidified a portion of the tin inside the crucible. By varying the current to the heater and the water flow rate to the pressure vessel, the amount of liquid tin in the crucible, and thus the position of the solidification front, could be varied. A set of 16 chromel-alumel thermocouples was mounted inside the crucible and used to monitor the location of the solidification front.

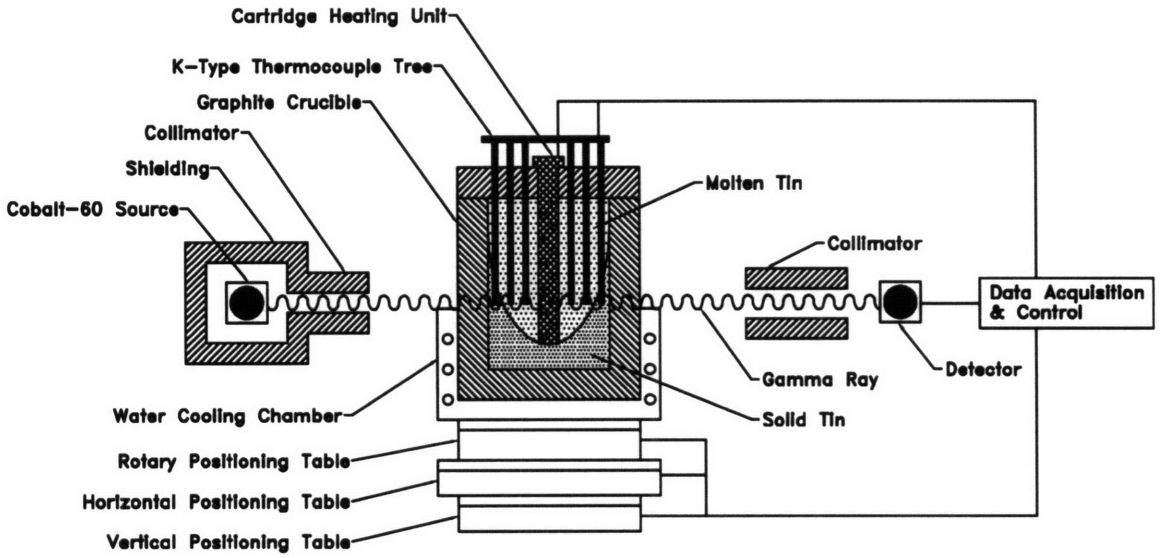

Figure 3.10 Schematic of two-phase metal experiment.

When the solidification front of the two-phase tin reached a quasi-steady state, the CT scans were begun with a STO distance of 215 mm, resulting in a total of 67 steps with the 1.9 mm step size for the transverse measurements and 60 view angles with 3° step size for the angular measurement. Even though the ratio of N_o to N_s was less than ideal due to an extremely long data acquisition time and the instability of the two phase state maintenance. A photon count time of 300 seconds produced a photon count range within the data set of 4629 to 25220, resulting in a photon count error of 0.63 to 1.47 %. During the course of the data acquisition, the temperatures of the 16 positions were recorded by the thermocouple at each photon count measurement as shown in Figure 3.11 (a). Because the data acquisition period for this experiment was 14 days, there must have been a tremendous amount of temperature fluctuation which significantly altered the location of the

solidification front over the course of the experiment. However, by taking the average of the thermocouple measurements, an estimate of the time-averaged position of the solidification front was made.

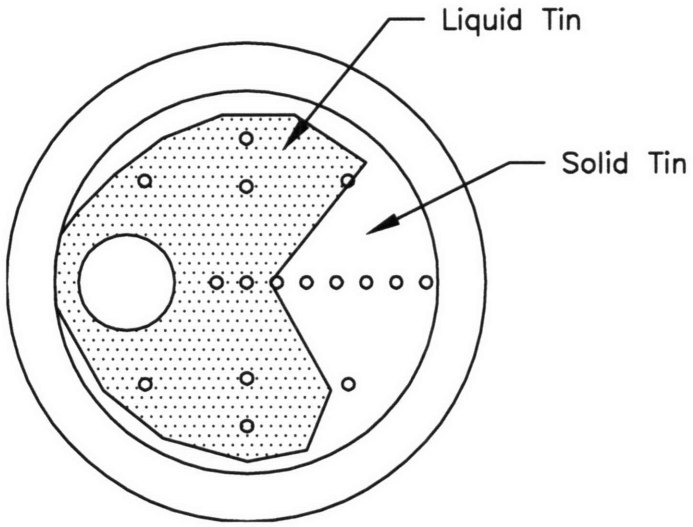

(a)

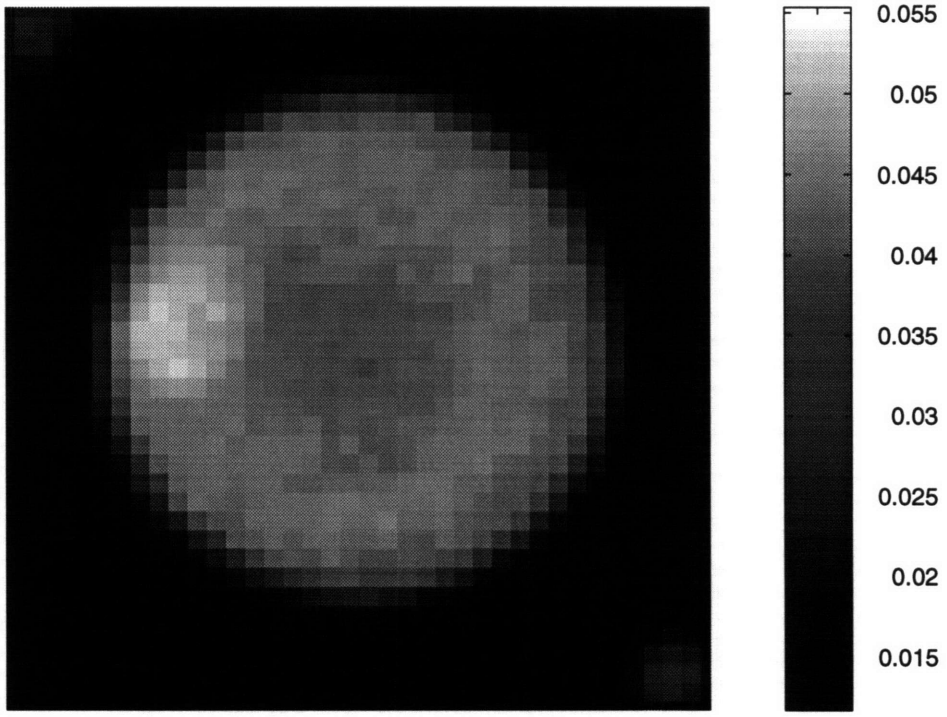

(b)

Figure 3.11 (a) Estimated solidification front position based on average thermocouple measurements, (b) Experimental solidification front position based on CT image. Numbers on the right hand side represent intensity.

Figure 3.11 (b) shows the reconstructed CT image of two-phase tin experiment with only the material inside the crucible as compared with an estimate of the liquid tin pool size based on the time-averaged thermocouple measurements. Comparison of the two images reveals a smaller liquid pool size present in the CT image than predicted by the thermocouple measurements because there were several sources of error. The largest source was the fluctuation in melt temperature because of the extremely long data acquisition time, for it is difficult to maintain a constant melt temperature even with a temperature controller. The second source of error was poor statistical count. The last source of error was undersampled data set which was deemed acceptable for the experiment since a higher ratio of the view angles to transverse scans would have further extended an already long data acquisition time. Because the experiment was plagued with many sources of error, the position of the solidification front could not be properly validated using the thermocouple measurements. However, a contrast difference in density between the liquid and solid tin phases inside the crucible is apparent.

3.7 Summary

Through the preliminary experiments, several findings and limitations of the CT system have been observed and the following conclusions can be made:

- Based on the Gamma-Ray attenuation experiment, the proposed concept of the radiation attenuation measurements is a viable method of determining the thickness of liquid or solid section of a solidifying casting.

- Comparison of the actual objects with the reconstructed images of an aluminum block, an aluminum cylinder, and a tin/steel composite cylinder confirms that the CT system can detect a density difference of 7 %.

- Despite a great deal of temperature fluctuation due to a long data acquisition time and a set of undersampled data, the reconstructed image of the two-phase tin shows a time averaged position of the solidification front and distinguishes a 4 % density difference between the liquid and solid phases.

- Due to the low photon flux produced by the Co^{60} radioisotope, this system does not have real-time capability. Alternatively, the use of a source with a large flux, such as an x-ray linear accelerator (LINAC) will dramatically decrease data acquisition time, possibly to the point of real-time performance.

- Applying a new reconstruction algorithm with limited view angle data may speed up the processing time when combined with known parameters, such as material density and geometry, which may make the real-time detection system viable.

CHAPTER 4

PRIMARY DESIGN CHARACTERISTICS FOR A HIGH-ENERGY TOMOGRAPHIC SYSTEM

Having satisfactorily demonstrated the feasibility of real-time monitoring of a continuous casting process by the computed tomography (CT) technique in Chapter 3, we now delve into the specifics of a generic tomography system. The fundamental issues and various design alternatives are present for each component, along with their performance. This chapter will provide a wide range of specifications for future reference and characterize the critical parameters of the CT system.

4.1 Source

The three types of radiation source typically used in industrial CT are x-ray tubes, γ-ray sources, and high-energy x-ray sources such as linear accelerators. An ideal radiation source should provide a high-intensity beam of x-ray photons at a single energy or optimum spectral spread, emanating from a very small area with an energy capable of transmitting a reasonable fraction of the x-rays through the object being scanned. Each of the three source types has advantages and disadvantages for use with our system, and would require careful optimization for practical application. A comparison of the candidate sources follows.

4.1.1 γ-ray source

A major advantage of a γ-ray source over an x-ray source is that the high-energy photons produced by the γ-ray source are at specific energies, or wavelengths, while an x-ray source produces photons over a wide spectrum of wavelengths. On the other hand, the primary disadvantage of a γ-ray source is the limited radiation intensity, as measured in number of photons produced per second. That is, the source strength is relatively weak. While the intensity can be increased by using more radioactive material, this requires a larger radioactive source, which adversely affects the spatial resolution of the tomographic

image. Also, because the energy of a γ-ray source is dependent on the type of isotope, the effective energy cannot be readily varied to suit the imaging system.

Table 4.1 Several gamma-ray radioisotopes.

Isotope	Energy [MeV]
Cobalt 60	1.33, 1.17
Cesium 137	0.66
Iridium 192	0.31, 0.47, 0.60

4.1.2 High energy x-ray source

The key characteristics of a high energy x-ray source include: operating voltage range, effective size of the focal spot, and operating power level. These characteristics are important in both radiography and CT. Stability of the x-ray source is especially important in CT. Voltage variations are particularly disruptive because they change the effective energy of the x-ray beam and consequently cause image artifacts. Current variations are less of a problem because x-ray intensity fluctuations can be monitored by reference detectors.

Some advantages of using a high-energy linear accelerator system in lieu of an isotopic sources such as Cobalt 60 or Iridium 192 include shorter exposure time, better image quality, and improved safety due to the absence of radioactive materials. The shorter required exposure time possible with a high energy linear accelerator compared with Co^{60} radiographs can be attributed to its higher penetrating energy and radiation intensity. For instance, MINAC 6, a 6 MeV accelerator operating at 300 rad per minute @ 1 meter with penetrating power equivalent to 20,000 Ci Co^{60}, can produce high-quality radiographs through up to 356 mm (14") of steel or up to 1,575 mm (62") of concrete. The practical limits of penetration using Co^{60} are much lower, at only 152 mm (6") for steel and about 457 mm (18") for concrete. Penetrating thicker sections with Co^{60} requires much shorter focal distances, which results in image quality degradation, and excessively long exposure times. The MINAC also has a smaller focal spot size (1.7 - 2.0 mm for MINAC versus 5.0 - 10.0 mm for Co^{60}), yielding images with sharper edge definition and better contrast (Schonberg Radiation Corporation, 1991).

Accurate and repeatable dose exposure is another advantage of a high-energy linear accelerator. Its inherent design is well suited for controlled exposure, with a dosimetry system that measures output dose rate at the x-ray target as well as total dose to the detector. This minimizes the number of trial exposures and enables easy exposure repeatability. Since the output dose rate at the target side diode sensor can be varied from 10 to 100% of the maximum controlling pulse repetition rate, total dose information from the detector-side ion chamber sensor is used to switch the machine off when the selected exposure level has been attained.

4.1.3 X-ray collimators

Collimators are radiation shields with open apertures that shape the x-ray beam striking the object and the detector. For CT systems, the radiation field is typically a thin fan beam wide enough to cover the linear detector array past the object being scanned. A collimator is located between the x-ray source and the object to shape the beam. Normally, a second collimator is also placed between the object and the detector array to further define the object volume being sampled. One or both of the x-ray collimators may have adjustable slot spacing to permit operator selection of the slice thickness. One of the benefits of using a thin fan beam of radiation for CT and Digital Radiography (DR) imaging is that most of the radiation scattered by the object misses the detector array and will not measured. This improves the quality of the measured data over those obtained by large-field radiography. Systems that use sparsely spaced detectors, such as multi-detector translate-rotate systems, may also have detector aperture width collimators. These collimators reduce the effective size of the detector element, thus improving the resolution of the transmitted data.

4.2 Detector

4.2.1 Detector characteristics

The ability to measure the transmitted x-ray intensity precisely and efficiently is critical to x-ray tomographic imaging. Features of the detector that are important to imaging performance are efficiency, size, linearity, stability, response time, dynamic range, and effective range of energy (Dennis 1992).

Detector efficiency is a quantitative measure of the effectiveness of the detector for intercepting, capturing, and converting the energy of the x-ray photons into a measurable signal. This efficiency is the primary factor in the image quality for a given x-ray source and the exposure time required to collect a sufficient amount of radiation. There are three distinct detector efficiencies: geometrical efficiency, collection efficiency and conversion efficiency. The geometrical efficiency is the fraction of the transmitted beam passing through the measured slice volume that is incident on the active detectors. It is equal to the active detector element width in the plane of the slice divided by the center-to-center spacing between detector elements. Collection efficiency is the fraction of the energy incident on an active detector area that is absorbed in the detector. It is dependent on the atomic number and density of the detector material and on the size and depth of the detector. Likelihood of detection decreases when x-ray photons pass through the detector without interacting or when the photon energy is lost due to scatter or characteristic x-ray emissions from the detector material. The third detector efficiency is conversion efficiency, which is the fraction of absorbed energy that is converted into a measurable signal.

Detector size consists of its width and height. The detector height determines the maximum slice thickness that can be measured. Increasing the slice thickness increases the collected x-ray intensity, thus reducing the image noise, but decreases the z-axis (interplane) resolution and may increase volume blurring and volume artifacts. The measured slice thickness is adjusted by the thickness of collimators that are less than the height of detector. The detector element width is a factor in determining the planar resolution of the tomographic image.

Detector linearity is the ability to produce a signal that is proportional to the incident x-ray intensity over a wide range of intensities. Detector stability is the ability to produce a consistent response to a signal without drifting over time, i.e., repeatability. To obtain solid channel-to-channel uniformity, consistency in signal response, noise, aperture size, and other characteristics are necessary for each detector element. These parameters are important in the tomographic detector selection process to produce consistent data set required for image reconstruction.

Detector response time is the time required for the signal to effectively settle without being significantly influenced by prior incident intensities. The response time is a critical factor in determining how rapidly independent samples can be collected.

Dynamic range is the range of intensities over which accurate measurement can be made. It is usually specified as a ratio of the maximum to the minimum signal output. The minimum signal output is limited by the electronic noise of the detector and its electronics. The level of electronic noise determines how the minimum signal can be effectively

sampled for processing by the computer. For film or real-time radiography, the dynamic range should not be more than a few hundred; for DR, the ratio of up to about 2000 are possible; and for CT, the ratio of up to 10,000 are acceptable and can even be exceeded in special circumstances.

Detector collimator is usually made out of a plate of high density substance, such as lead and tungsten, in which a large array of apertures are drilled. The purpose of the collimator is to geometrically confine the direction of incident photons reaching the scintillation crystal, thereby localize the site of the emitting sources. Most of the collimators are all parallel to each other because it provides the ideal combination of resolution and sensitivity for most regions of the object with no geometrical distortion. In some applications the apertures may be angulated to form converging or diverging hole collimators. Converging collimators have certain advantages in imaging relatively small regions while diverging collimator has those for relative large regions with appropriate magnification or reduction of the images. Alternatively, just one or a limited number of holes may be used to form a pinhole collimator which is particularly useful in imaging very small regions.

Collimator resolution, contributions to the resolution from the collimator depends on the design of the collimator including the shape, width, and length of the apertures and the distance of the region being imaged from the collimator. Collimator resolution, R_c may be defined in terms of the point spread function as:

$$R_c = \frac{W(L+D)}{L} \tag{4.1}$$

where W and L are the width and length of an aperture within the array of apertures, and D the distance of the point source from the outer surface of the collimator. Typically the collimator resolution is approximately 10 mm at a distance of 100 mm from the collimator.

4.2.2 Scintillation detectors

Scintillators. X-ray radiation causes electrons in the atoms of the absorbing material to be excited or ejected from the atom. These excited electrons rapidly recombine with the atoms and return to their ground-state configuration, emitting a flash of visible light photons in the process. Scintillation detectors typically use relatively large transparent

crystals. The scintillator is encased in a light-reflective coating and is optically coupled to a sensitive light detector, such as a photomultiplier tube or a photodiode.

Sodium iodide doped with thallium [NaI(Tl)] coupled to a photomultiplier tube is the standard scintillation detector used for nuclear radiation measurements. However, new scintillating materials have resulted in improved performance for certain detector characteristics. The scintillation materials of choice are cadmium tungstate ($CdWO_4$) and bismuth germanate (BGO). The properties of the material are important to the efficiency and speed of the detector and its ability to provide accurate data.

Table 4.2 Scintillator materials.

Material	Density kg/m^3	Index of refraction	Decay constant, μs	Photoelectron yield photons/MeVγ	Afterglow % at 3 ms
NaI(Tl)	3670	1.85	0.23	1.0×10^4	0.5 - 5
CsI(Tl)	4510	1.8	1.0	4.5×10^3	0.5 - 5
BGO	7130	2.15	0.3	$1.5\text{-}2.0\times10^3$	0.005
$CdWO_4$	7900	2.2	0.5 - 20	$2.5\text{-}3.0\times10^3$	0.0005

Table 4.1 lists some of these materials and their key properties. The relatively high density and effective atomic number are key attributes of many scintillator materials, which are designed to absorb the x-ray photons. The principal decay constant is the time for the signal to decay to 37% of the maximum. Afterglow is defined as a detrimental property of a scintillator in which the emission of light continues for a period of time after the exciting radiation has been discontinued. Long afterglow decay constants, i.e., from 1 to 100 seconds, in NaI(Tl) is one of its significant deficiencies for high-speed data acquisition. In addition to afterglow, the scintillator materials may also exhibit temporary radiation damage such as reduced optical transparency, with an associated time constant for repair. The effect of prior radiation exposure on the measured signal is especially important when a wide range of intensities is to be measured by the detector. The average number of photoelectrons produced per MeV γ-ray photon is also listed above. A high index of refraction increases the difficulty of optically coupling the scintillator. Careful selection and characterization of the scintillation detector material are necessary for high-speed CT data acquisition.

Photomultiplier Tube. A photomultiplier tube is a vacuum tube with a photocathode that produces free electrodes when struck by light. These electrons are accelerated and then strike positive electrons called dynodes, which release additional free electrons. A series of dynodes is used to obtain very high levels of amplification with low background noise.

Scintillation Crystal-Photodiode Array Detector. It has important advantages over photomultiplier tube in CT applications. Although photomultiplier tubes are relatively efficient, they are subject to gain drifts and are relatively bulky. Crystals with photodiodes are more stable and permit the use of small, tightly packed detector arrays. Therefore, photodiodes are commonly used as the optical sensor for CT scintillation detectors. Photodiodes produce a small current when light strikes the semiconductor junction. This current is then amplified by a low-noise current-to-voltage converter to produce a measurable signal. Very high resolution detector systems have been fabricated by coupling thin slabs of scintillation material to high-resolution photodiode arrays. These photodiode arrays may have 40 or more individual photodiodes per millimeter on a single chip.

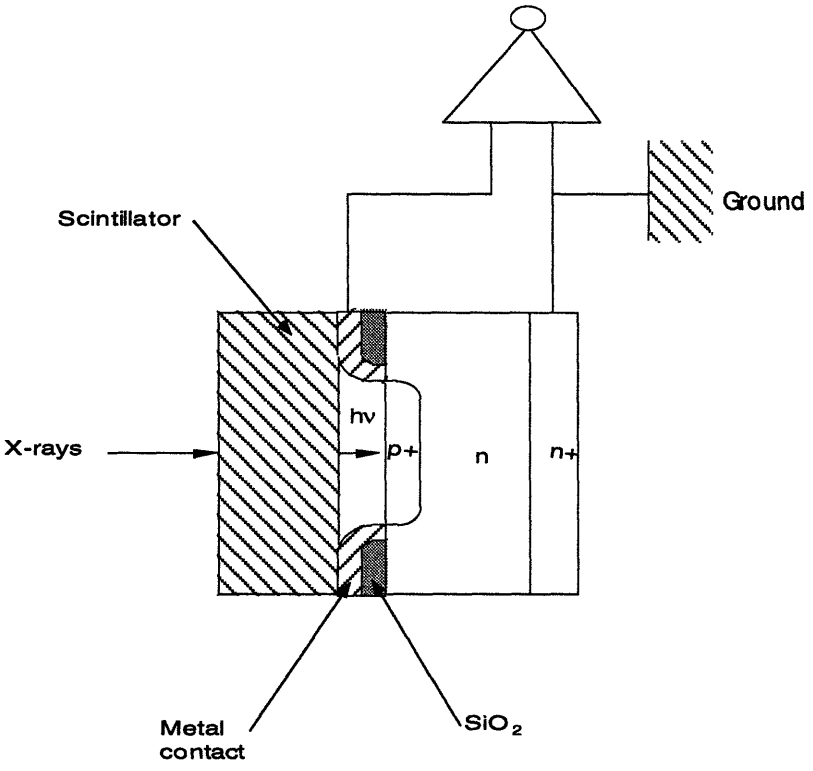

Figure 4.1 Scintillation crystal-photodiode detector.

Quantum Noise (Mottle) and the Detective Quantum Efficiency. Measured beam intensity consists of a finite number of photons. Even with an ideal detector, repeated measurement contains a certain degree of random variation, or noise. The standard deviation of the number of photons detected per measurement is $\sqrt{N}$, where N is the average number of detected photons per measurement. Therefore, the signal-to-noise (SNR) can be given by:

$$\text{SNR} = \frac{N}{\sqrt{N}} = \sqrt{N}. \tag{4.2}$$

Just as fast films that require less exposure tend to produce grainy images, the fewer the number of photons detected, the lower the signal-to-noise ratio. Because this type of noise is due to the measurement of a finite number of discrete particles, or quanta, it is referred to as quantum noise.

Because practical radiation detectors are imperfect devices, not all x-ray photons are absorbed in the detector. In scintillation detectors, a finite number of light photons reach the light sensor, and a finite number of electrons flow in the sensor. Each of these steps has its own quantum noise. The detector electronics, particularly those in the initial amplifiers, introduce additional noise into the measured signal, adding to the quantum noise.

The overall efficiency of the detector can be characterized by comparing its performance to that of an ideal detector. The detective quantum efficiency (DQE) of a detector is the ratio of the lower x-ray beam intensity needed with an ideal detector to the intensity incident on the actual detector for the same signal-to-noise ratio. If the only increase in noise versus an ideal detector is due to the absorption efficiency, that is, the fraction of photons absorbed in the detector, the DQE would equal the absorption efficiency.

Other losses of the signal occur in the detection process, and other sources of noise can be introduced into the signal to further reduce the SNR for actual measurements. The result in the quality of the measured signal is effectively the same as detecting fewer photons. The DQE can be determined by comparing the measured SNR to that calculated for an ideal detector as:

$$\text{DQE} = \frac{\left(\text{SNR}_{\text{det}}\right)^2}{\left(\text{SNR}_{\text{ideal}}\right)^2}. \tag{4.3}$$

Designers of CT detector systems strive to maximize overall detector efficiency while satisfying the size, speed, stability, and other operational requirements of a practical CT system.

4.2.3 Geometry of source and detector

The selected resolution decides the x-ray source spot width and the detector aperture width. While the spot width is restricted to what is available from the manufacturers, the detector width can be chosen more freely. The ideal case is when the two are approximately the same, and the object is half-way between the source and detectors. The best resolution then corresponds to a width about half that of either. Otherwise, the object should be placed as close to the smaller width as possible, determining the resolution. The ratio of distances from the object to the source and to the detector should be about the same as the ratio between their widths.

4.2.4 Scatter radiation

The three main mechanisms of the gamma radiation interactions include photoelectric effect, Compton scattering, and pair production. These are functions of photon energy and incident material, as shown in Figure 4.2.

Over the energy range 0.01 to 10 MeV, the radiation incident on the metal interacts in two principal ways to attenuate a beam of radiation (Evans, 1955). First is the photoelectric interaction which is strongly dependent on the atomic number of the element and on the energy of the gamma radiation. Second is the Compton interaction, which is only dependent on the electron density of the material and weakly on energy. Therefore, it is dependent only on the mass of the material, not on its elemental composition. The photoelectric interaction is strongly energy dependent and decreases rapidly with energy. It is thus only important at low energies. However, at high energy, which is the range ofinterest for the proposed application, the scattered radiation due to the Compton interaction dominant. Therefore, scattering is one of the important issues to be considered.

Detected scattered radiation produces a false detection signal which does not correspond to the transmitted intensity along the measured path. The amount of scattered radiation detected is much lower than that encountered with large-area radiographs because

of the thin fan beam normally used in the CT. The CT sensitivity, however, makes a potential problem even at low levels of scatter.

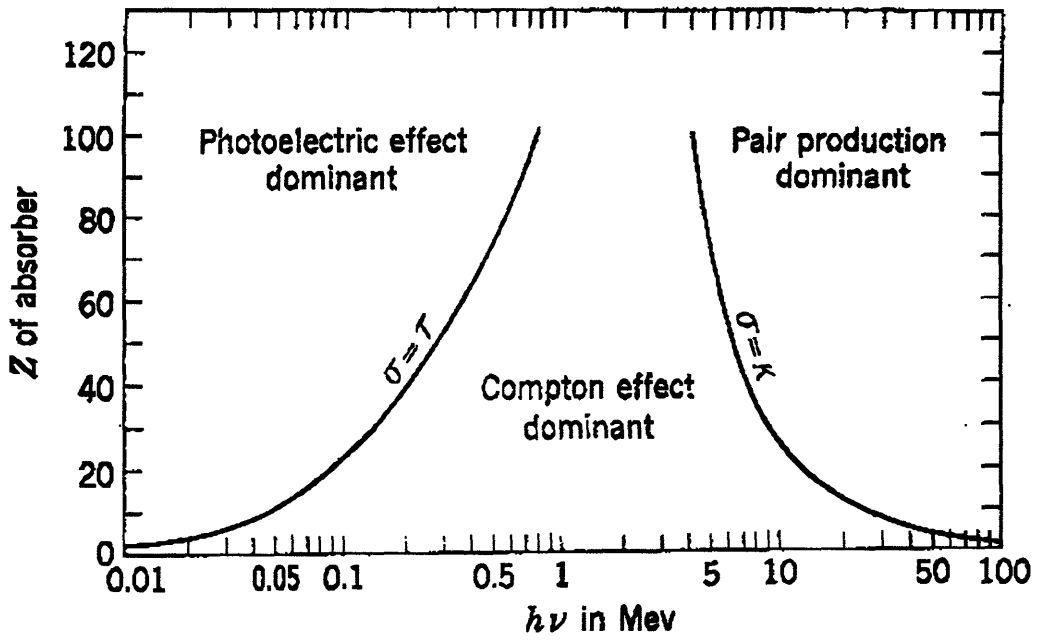

Figure 4.2 Relative importance of the three major types of γ-ray interaction for various energies (Evans, 1972).

The scatter contribution across the detector array tends to be a slowly varying additive signal. The effect on the measured data is most significant for highly attenuated rays, in which the scatter signal is relatively large compared with the primary signal. The additional measured scattered photons make the materials along the measured path appear less attenuating. It is the same effect caused by beam hardening, which will be discussed in Section 4.6.3.

The types of artifacts caused by scatter radiation are similar to and often associated with beam hardening. In addition to the cupping-type artifact, beam hardening and scatter can also cause broad, low CT number bands between high density structures. The rays that pass through the high-density structures are highly attenuated, and the increase in effective energy and the scatter signal makes the materials along the these path appear to be less attenuating than is determined from other view angles. The amount of scatter radiation detected can be modeled, and specific scatter correction processing can be implemented.

A careful system design can also minimize the detected scattered radiation. A tightly collimated, thin x-ray beam minimizes the amount of scatter radiation produced. Increasing the distance between the object and the detector decreases the fraction of the

scatter radiation detected. The use of focused collimators or directionally sensitive detectors also reduces the amount of detected scatter radiation. Because the scatter radiation varies slowly with distance, special reference detectors outside of the primary radiation beam can be used to measure the level of the scatter signal and nullify its effect.

4.3 Actuator

4.3.1 General configuration and evolution of the CT system

CT scanning geometry is very important to acquisition of the necessary transmission data. In general, many closely-spaced transmission measurements with a number of angles are needed. Four generations of CT scanning geometries are shown in Figure 4.3. In CT systems, either the object or the radiation source and detector can be moved since the relative positions of the object to the measured ray paths are equivalent.

Single-Detector Translate-Rotate Systems. The first commercial medical CT scanner used a detector to measure data in a cross section. In this CT scanner, the x-ray source and detector are mounted on parallel tracks. The source and detector traverse past the object in a linear fashion and make a series of x-ray transmission measurements. These measurements correspond to the transmitted intensity through the object along a series of parallel rays. The source-detector assembly is rotated by certain fixed amount, after which another linear translation is made. This provides another set of parallel rays at a different angle. This process is repeated until data are obtained over a full 180° rotation of the source-detector system.

Single-detector translate-rotate CT system are often referred to as first generation systems. Medical manufacturers use this nomenclature to emphasize the different stages of their design and to describe the different CT system operation. Current CT system do not employ this single-detector approach due to its low throughput. However, the simplicity of this system makes it suitable for basic research.

Multi-detector Translate-Rotate Systems. Multiple detectors can be used to improve data acquisition speed by generating various simultaneous transmission measurements. Multi-detector translate-rotate systems, or second-generation systems, use a series of spacing detectors to produce simultaneous x-ray transmission profiles from various angles. The data are still obtained during the translation motion, but the system is

rotating at a larger increment. The translation distance must be somewhat longer than that of a signal detector system in order to allow all source-detector rays to pass over the width of the entire object, but fewer translations are needed to collect a full set of data. The second-generation CT scanning geometry is suitable for industrial applications.

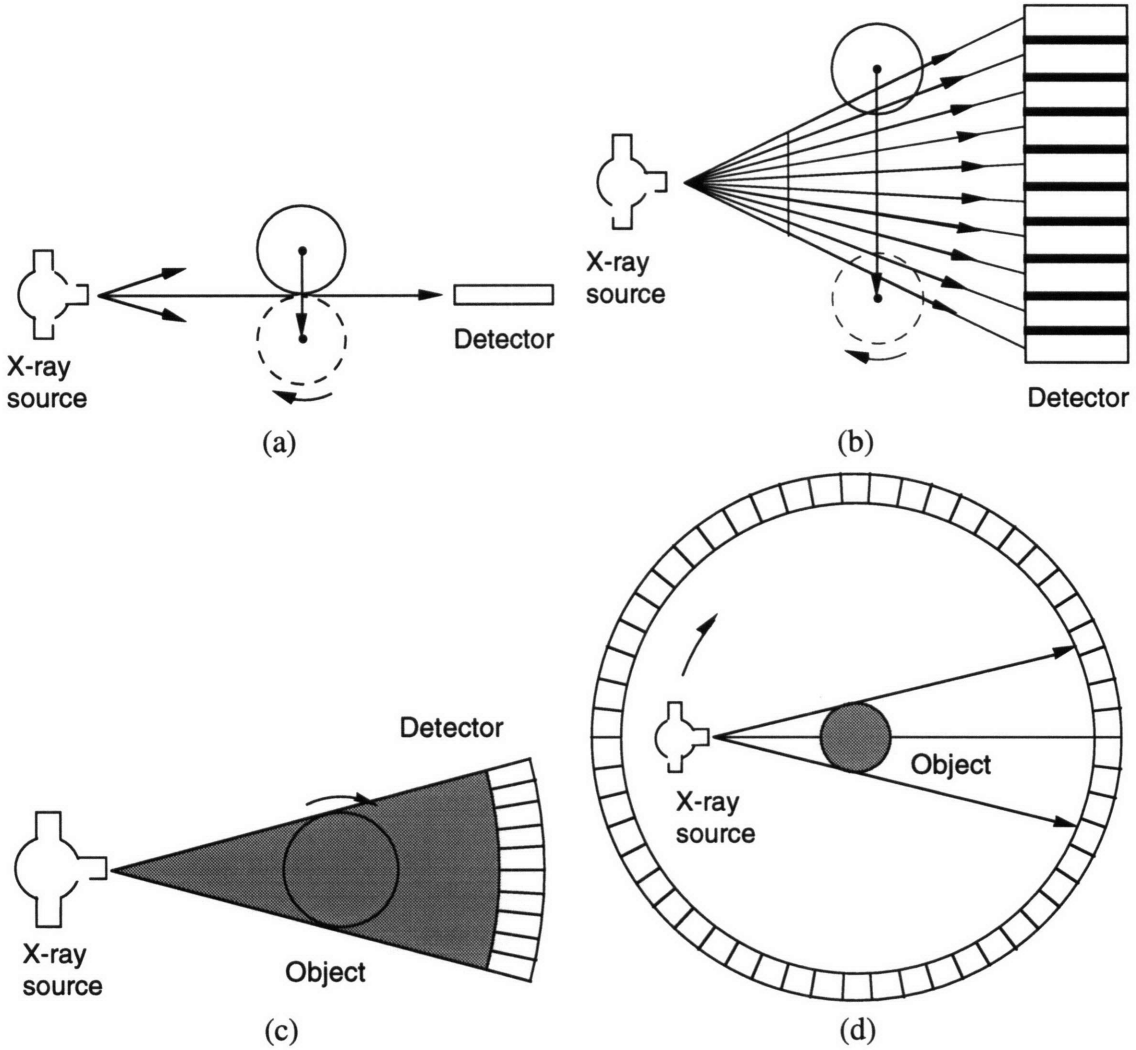

Figure 4.3 CT scanning geometries: (a) Single-detector translate-rotate, (b) Multi-detector translate-rotate, (c) Rotate-only, and (d) Stationary-detector rotate-only (Dennis 1992).

Rotate-Only Systems. Additional improvement in data acquisition speed can be achieved by employing a broad fan beam of radiation spanning the entire width of the object, eliminating the translation motion entirely. Nearly, all current medical scanners are rotate-only systems and some make over 1 million transmission measurements for a complete scan in less than 2 seconds.

Rotate-only systems have two primary configurations. Third generation systems use many closely-spaced detector elements that are fixed relative to the x-ray beam. Each projection path is defined by a matching detector. Because the entire object is encompassed by the detector array, no translation is necessary. Therefore both the source and the detector array require only simple rotation around a fixed center. The entire 360^{o} is usually scanned to collect all of the transmitted data. The scan time can be as short as 1 to 3 seconds. The major drawback is the cumulative effects of the detector drift, appearing as artifacts in the reconstructed image.

The fourth generation systems contain a stationary ring of detectors that encircle the object, and the x-ray source rotates around the object. In the fourth generation systems, the x-ray fan beam exposes only a portion of the detectors at any given time. Data are usually regrouped into fan beam sets, with the detector at the apex of the fan, or into an equivalent parallel ray set. With this kind of configuration, the detector drift is not cumulative and therefore can be corrected. Benefits of this system are similar to the third-generation systems, but the major drawback of the third generation systems, the drift effects, has been eliminated. This configuration, however, is often less flexible and more expensive because the large number of scintillation detectors. It cannot manipulate the object, and is normally not suitable for use in industrial systems.

4.3.2 Characteristics of each generation and factors for suitable choice

Each of the CT scanning geometries has its advantages and limitations. There are many factors in determining image resolution such as source strength, source-object and object-detector distance, detector aperture, and reconstruction algorithm. One of the primary factors is the spacing between the measured transmitted rays. The resolution at the center of the image field and in the radial direction at the periphery is mainly dependent on the ray spacing in a transmission profile. This ray spacing can be easily adjusted for the linear distance moved between measurements during the translation. In the third generation systems, this ray spacing is fixed by the spacing, well below 1 mm of the densely packed detector array elements. The ray spacing through the object can be improved by moving the object closer to the γ-ray source or by acquiring interleaving data over multiple rotations with the detector array shifting a fraction of the detector spacing.

The circumferential resolution at the periphery of the image is dependent on the angular step size between views and the diameter of the image field. The rotate-only

system has the advantages in readily adjusting the number of angular views acquired and the ray spacing along the circumference. In the second generation (multi-detector translate-rotate systems) system, the angular step size is fixed by the detector array spacing. This system also can adjust the translation distance by the length of the object diameter plus the width of the fan beam at the object position. This might be inefficient for a wide fan beam system with small objects, but gives considerable flexibility with large objects.

In the rotate-only systems, the source-object and object-detector distances (object magnification) and the size of the detector array determine a field-of-view. If the detector array size dose not cover the whole field-of-view, the fan beam data are still acquired by shifting the detector during translation motion, i.e., the rotate-shift-rotate approach or by translating the object. Even for higher resolution, interleaved data can be obtained by repeating the rotational scan with a shift of a fraction of the detector spacing. Furthermore, for large objects, a scan-shift-scan approach can be used.

There is considerable flexibility for various requirements. Each system's capabilities depend upon mechanical parts and implementation of the particular data acquisition to determine the efficiency of the system in acquiring appropriate data as well as the subsequent imaging throughput.

4.4 Data Acquisition System and CT Computer System

4.4.1 Data acquisition system

The data acquisition system is the electronic interface between the detector system and the computer. It provides further amplification of the detector signals, multiplexes the signals from a series of detector channels, and converts these analog voltage, or current signals, to a binary number that is later transmitted to the computer for processing. Key characteristics of this electronics package are low noise, robust stability, calibration of offset and gain variations, linearity, sensitivity, dynamic range, and sampling rate. The electronics of the data acquisition system should be well matched to the detector system in order to minimize degradation of data accuracy and scanning performance.

The dynamic range of this detector system is characterized by the maximum SNR. The dynamic range of the data acquisition system is obtained by the range of numbers that can be transmitted to the computer, often specified by the number of bits per measurement. CT systems often have a dynamic range of 20 bits (2^{20}, or 1×10^{6}).

4.4.2 CT computer system

CT imaging has improved due to the computational advancements that have permitted increasing amounts of transmission data to be measured to produce larger, more detailed image matrices at increased speeds. High-speed computer systems also have enabled increasingly sophisticated data processing techniques for image enhancement, alternate data presentations, and automated analysis. Because CT employs large amounts of data (millions of transmission measurements to produce an image containing up to several million image values) and several billion mathematical operations are required for image reconstruction, high-speed array processors are necessary for image reconstruction. Array processors are special-purpose computer processors to perform special functions at high speeds. They are very efficient devices for performing standard vector or array operation. The CT reconstruction technique commonly used also requires a backprojection operation in which projection values are mapped back into two-dimensional image matrices. Consequently, most CT systems contain specialized processors that perform this operation efficiently in addition to standard array operations. In addition, careful handling and archiving of data are required due to the enormous amount of collected data.

4.5 Computed Tomography

X-ray Computed Tomography (CT) provides quantitative, readily interpretable data that enables the inspection of structures not amenable to other nondestructive evaluation techniques. CT has become well established as an inspection, evaluation, and analysis tool in industry. Many of the applications have been in aerospace industry, where the high cost and performance requirements of components justify the cost of CT inspection, but use in other industries is growing as the equipment becomes increasingly available.

4.5.1 Advantages of CT over radiography

Tomography is an image of a single slice taken through a three-dimensional object while radiography is a superposition image from all slices, equivalent to a projected image. X-ray CT provides a cross-sectional view of the interior of an object. CT is distinguished from conventional radiography and radioscopy by the different orientation of the image

plane, and by the nature of the data. The primary performance characteristics of each system are compared in Table 4.2. Conventional planar imaging techniques used in radiography suffer from artifacts and errors due to superposition of underlying and overlying objects that interfere with the region of interest and are limited due to the very nature of the image production. Variations in density as observed in the image represent the integrated interaction cross-section over the entire path of the radiation through the object. Details of internal structure and embedded objects are easily hidden by this effective averaging. Although more information may be obtained by taking projection views from different angles in order to achieve a stereo-like effect, the basic limitations are still present. Tomography using the method of image reconstruction from projections allows two- and three-dimensional detail to be retained and visualized in cross-section, retaining the spatial distribution of the radiation attenuation coefficients and thus details of the internal structure. The technique is well known from its application to medical imaging and extension to casting applications is straightforward.

Tomographic reconstruction methods are well known and these techniques can also be applied to those cases where the number of viewing angles is limited, so called "limited angle reconstruction."

Table 4.3 Comparison of the performance characteristics of film radiography, real-time radiography, and x-ray computed tomography (Dennis, 1992).

Performance Characteristic	**Film Radiography**	**Real-time Radiography**	**Computed Tomography**
Spatial resolution	>5 line pairs/mm	2.5 line pairs/mm	0.2-4.5 line pairs/mm
Absorption efficiency, %			
80 keV	5.0	20.0	99
420 keV	2.0	8.0	95
2 MeV	0.5	2.0	80
Sources of noise	Scatter, poor photon statistics	Scatter, poor photon statistics	Minimal scatter
Dynamic range	200-1000	500-2000	Up to 10^6
Digital image processing	Poor; requires film scanner	Moderate to good; typically 8-bit data	Excellent; typically 16-bit data
Dimensioning capability	Moderate; affected by structure visibility and variable radiographic magnification	Moderate to poor; affected by resolution	Excellent; affected by resolution, enhanced by low contrast detectability

4.5.2 Beam geometry

The beam of radiation in CT may be a narrow pencil beam, a fan shaped beam, or a cone beam originating at a LINAC. The choice depends on the required speed and number of detectors to be used. The reconstruction techniques for pencil and fan beams are identical while reconstruction for cone beam is different.

Several options exist for scanning the object, i.e., the casting in this case.(Chun, 1994) In the simplest method, a single pencil beam and a single detector are translated across the casting to make measurements. The entire assembly can be moved vertically to produce a complete scan, which is shown in Figure 4.4.

Figure 4.5 shows a scanning technique in which the radiation source is still a pencil beam but in which the pencil beam is rotated across the casting while the detector moves. This method is more practical when the physical size of the radiation source is large.

Figure 4.6 shows a beam configuration in which the beam from the radiation source is in a fan shape. There are several ways in which this may be used. If a single source position is used with multiple detectors, the speed of the measurement may be increased by a factor equal to the total number of detectors. Furthermore, by moving and rotating the source, multiple beams may be overlapped to form a tomographic image. The number and spacing of the beams may be chosen using well known methods to produce images of the desired spatial resolution.

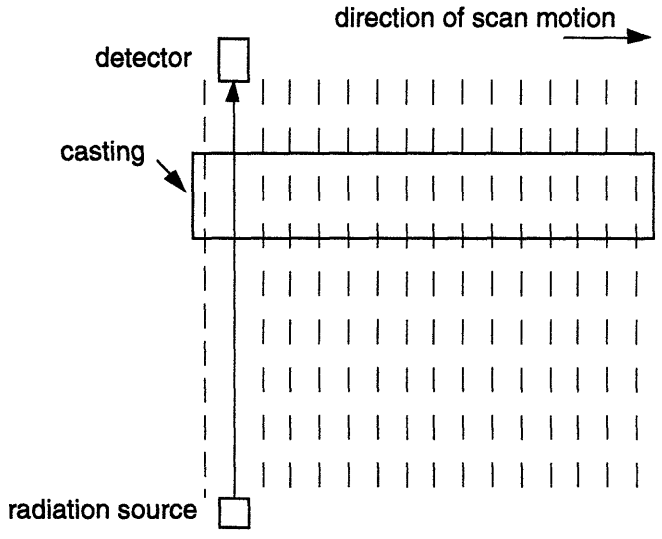

Figure 4.4 Parallel pencil beam scanner.

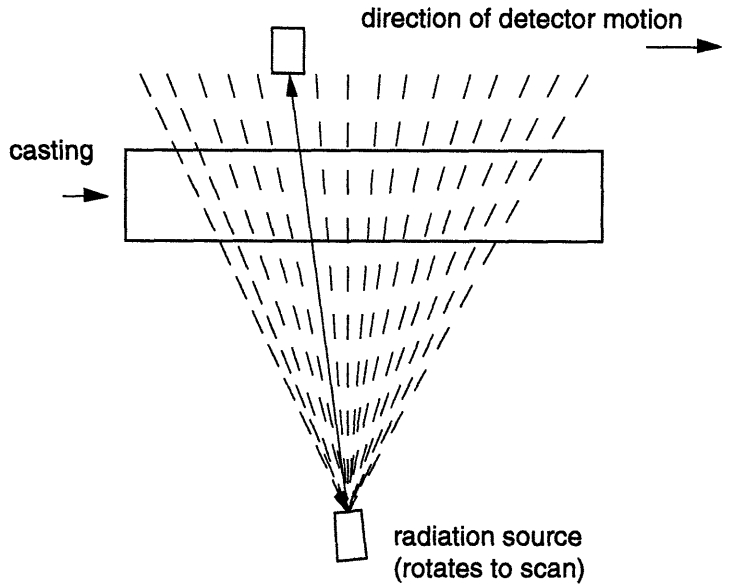

Figure 4.5 Single pencil beam with detector motion and rotating source.

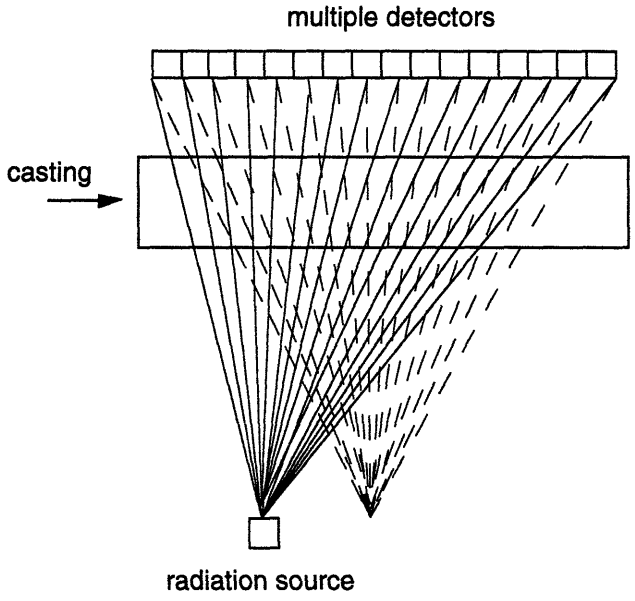

Figure 4.6 Use of fan beams to produce tomographic images. Two positions of the radiation source are shown producing overlapping beams for tomography.

The use of a thin fan beam with a slit-scan data acquisition is a very effective method of reducing the relative amount of measured scatter radiation. This can significantly improve the overall image contrast.

The earliest convergent collimators were configured as a stack of fan-beam collimators, one for each transaxial plane. This arrangement leads to improved sensitivity transaxially but not axially. In order to obtain the best sensitivity, the collimator should be convergent in both the axial and transaxial directions. This is achieved using a cone beam geometry. The two main approaches to the reconstruction of cone beam CT images are classified as direct and iterative. The direct methods are based on an inversion formula derived from the formulation of the problem in terms of line integrals through the desired image. Although these methods do not take account of important factors such as attenuation, detector response, and noise, they provide reconstruction in a relatively short time. The iterative methods are able to include a full statistical model for the data and may directly include all the factors. This improvement in the modeling, and consequently in image quality, is achieved at significantly increased computational costs.

Table 4.4 Comparison of fan beam geometry and the cone beam with three-dimensional reconstruction using CCD camera and screen.

	Advantage	Disadvantage
Fan Beam	• Less scatter • Efficient detector ($CdWO_4$, ρ=7900 kg/m^3) • Simplest	• Longer acquisition time since two dimension
Cone beam with 3D reconstruction using CCD and screen	• Short acquisition time	• Noise due to scattering • Low detection efficiency of screen (thin and low ρ) • Loss of photons from screen to CCD • Difficult computer intensive reconstruction • Difficult source movement

The image reconstruction problem for cone beam geometry is different with that for the parallel and fan beams. The major difference is that in the latter case rotating the source once around the object provides a full set of projections, from which theoretically the image can be exactly reconstructed. In contrast, rotation of a cone beam collimated source around the object provides insufficient data to exactly reconstruct the image. The advantages and disadvantages of the fan beam and cone beam with the charged coupled device (CCD) camera are generally listed in the table 4.3. While the operations differ for parallel and cone beam geometry, the mathematical details of the algorithms are independent of the data collection geometry. Therefore cone beam images can be reconstructed using the iterative

algorithm which is used currently. However, since cone beam tomography is a truly three-dimensional imaging modality, the problem cannot be decomposed into a set of two-dimensional reconstruction problems, as can the parallel problem. The computational cost involved in performing multiple forward and backward projections is prohibitively high.

4.5.3 Data requirements for proper CT image reconstruction

Since CT image reconstruction is performed based on limited data, appropriate data collection is of great importance. For proper image reconstruction for the Filtered Back Projection (FBP) reconstruction algorithm, the relationship between the number of view angles, N_θ and the number of transverse measurements, N_s is:

$$N_\theta \geq \frac{\pi}{2} N_s. \tag{4.4}$$

This relationship was applied in preliminary experiments and proved its usefulness. As seen in equation (4.4), the lower bound on the number of angular steps is proportional to the number of translational movements by the constant scalar factor of $\pi/2$.

4.6 Image Quality

To evaluate and monitor the image quality and performance of an imaging system, some basic criteria are required to characterize the resolution, sensitivity, and accuracy of a system. The several main factors affecting image quality and performance of an imaging system are spatial resolution, contrast, and artifacts (Dennis, 1992).

4.6.1 Spatial resolution

Spatial resolution is a criterion of the ability of an imaging system indicating how small details are distinguished. In CT, a bar pattern resolution test is used, while a line pair gauge is used for radiography. A CT resolution bar phantom consists of a stack of alternating high- and low-density layers of decreasing thickness. This phantom is scanned such that the layers are perpendicular to the slice plane. The resulting CT image displays a

bar pattern, and the minimum resolvable bar size (layer thickness) is determined. This measurement can be reported as the bar size or as line pairs per millimeter. Alternatively, resolution hole patterns can be used. This type of phantom is a uniform block of material (usually cylindrical) containing a series of drill holes. The holes are often arranged in rows, with the hole spacing twice the hole diameter. Hole patterns can also be placed in test specimens to demonstrate resolution in the materials to be scanned. As with the bar pattern, the minimum resolvable hole size is used as a measurement of the resolution. Comparing the two patterns, the bar patterns generally indicate a higher-resolution performance than the hole patterns, probably because of the improved perceptibility of the larger structures.

The image produced by a system is a blurred reproduction of the actual object distribution. A more complex way of characterizing resolution and reproducing the object structure is by measuring the degree of image blurring or the Point Spread Function (PSF) of the system. The PSF is the image response to a very small or point-like feature. This measurement can be made on a CT system by imaging a fine wire oriented perpendicular to the slice plane. If the pixel spacing is close to the resolution of the system, the extent of the PSF may extend for only a few pixels and be poorly characterized. The PSF can also be determined from measurements of the line spread function (LSF) or edge response function. The LSF is a normalized plot of the image across a line, such as a very thin sheet of metal oriented perpendicular to the slice plane. The edge response function is the plot of the image across a low-density to high-density boundary.

It is helpful in making LSF and edge response function measurements to orient the line or edge slightly out of alignment with the columns of displayed pixels. By determining the relative position of data from several rows, one can obtain a finer sampling of these functions. These functions can be partially characterized as a single parameter by reporting the full width at half the maximum value of the spread function.

One of the primary factors affecting resolution is the spacing between the measured transmitted rays. This ray spacing is easily adjusted in translate-rotate systems by adjusting the linear step distance during the translation. However, its effect is significant on the resolution at the center of the image field and in the radial direction at the periphery. Source size, detector aperture, degree of geometric magnification, and the reconstruction algorithm are other factors that affect resolution.

Practical measurements are made with radiation sources of a finite size and a detector with a definable aperture width. A single transmission measurement is therefore a type of average over a ray of some width. This ray profile is dependent on the size and shape of the focal spot, the width of the detector aperture, and the relative position between

the source and the detector. An approximation to the effective beam width, known as the effective aperture size, is given by:

$$\text{Beam Width} = \frac{a^2}{M^2} + \frac{s^2}{\left[M/(M-1)\right]^2} , \tag{4.5}$$

where a is the detector aperture and s is the width of the γ-ray focal spot. The variable, M, is the magnification factor given by:

$$M = \frac{\text{source} - \text{detector distance}}{\text{source} - \text{object distance}} . \tag{4.6}$$

As magnification increases, it is increasingly more important to have a small source to produce a high-resolution image. If the sampled data are at a finer spacing than the effective aperture, deconvolution processing of the measured data can reduce the effective aperture somewhat, but the result will be a noise increase in the data. Sample spacing through the object below one-half the effective aperture, however, have little benefit because of the lack of appropriately detailed (high-frequency) information in the measurements.

The Nyquist sampling theorem states that sampling frequency must be at least twice the maximum spatial frequency of the structure being measured. For example, in case of the bar resolution pattern, two samples per millimeter are required to define the one line-pair per millimeter bars.

While the translational step size within a view is the limiting resolution factor in the radial dimension from the center of the image, the circumferential resolution, perpendicular to the radius, is primarily associated with the angular step size. Therefore the larger the diameter of the object, the larger number of angular views are required to maintain a given circumferential resolution at the edges.

The measured transmission values are processed by a reconstruction algorithm to obtain the image, with FBP being the common method. The filter function in this process and image post-processing like image smoothing to minimize the image noise are obviously additional factors affecting the system resolution. Besides, part of the reconstruction process is the backprojection of the projection data into the image matrix. Since the rays corresponding to the measured data generally do not pass through the center of each affected pixel, interpolation between measured values is required. The method of interpolation can also affect the image resolution and noise. Thus, appropriate system

design and scan parameter selection are required for optimizing image quality since many factors affect the final resolution of the image.

4.6.2 Contrast

The degree of contrast on a CT image is governed by object contrast, detector contrast resolution, and spatial resolution of the system. Object contrast refers to the contrast generated by variations in the attenuation of the radiation propagating through the object. It is a function of the difference in the linear attenuation coefficients. Since the linear attenuation coefficient is affected by the γ-ray energy and material density, object contrast directly depends on the energy of the γ-ray source. The relative contrast between the object and the surrounding background material is the normalized difference between the two linear attenuation coefficients:

$$\text{Contrast}(\%) = \frac{\mu_{\text{object}} - \mu_{\text{background}}}{\mu_{\text{reference}}} \times 100, \tag{4.7}$$

where μ_{object} and $\mu_{\text{background}}$ are the linear attenuation coefficients of the object and the background material, respectively. The reference coefficient, $\mu_{\text{reference}}$, is normally that of the background material, but the larger of the two materials coefficients can be used, especially if the background material is air or has a very low relative value.

At high energy, while noise is reduced and measurement time can be shortened due to the strong photon transmission, contrast resolution is poor compared with the low energy range since there is no large variation between the linear attenuation coefficients of different materials.

4.6.3 Artifacts

Artifacts are image features which do not correspond to physical structures in the object. All imaging techniques are subject to certain types of artifacts. CT imaging can be especially susceptible to artifacts because it is sensitive to small object differences and each image point is calculated from a large number of measurements. Generally, two major causes of the CT image artifacts are the finite amount of data for generating the reconstructed image and the systemic errors in the CT process. Some of the factors that

can cause the generation of artifacts include inaccuracies in the geometry, beam hardening, aliasing, and partial penetration.

X-ray sources like a LINAC produce radiation with a range of photon energies up to the maximum energy of the electron beam. The lower-energy photons tend to be less penetrating and are attenuated to a greater degree by an object than the higher energy photons. Consequently, the effective energy of a beam passing through a thick object section is higher than that of a beam passing through a thin section. This preferential transmission of the higher-energy photons and the resulting increase in effective energy is referred to as beam hardening. Changes in the effective energy of the x-ray beam due to the degree of attenuation in the object cause inconsistencies in the measured data. X-rays that pass through the center of a cylindrical object will have a higher effective energy than those traversing the periphery, which leads to a lower measured linear attenuation coefficient. Thus, the center of a reconstruction image has lower number values. This CT number shading artifact is referred to as cupping, corresponding to the shape of a plot of CT numbers across the object. Figure 4.7 shows the effect of the beam hardening, i.e., cupping.

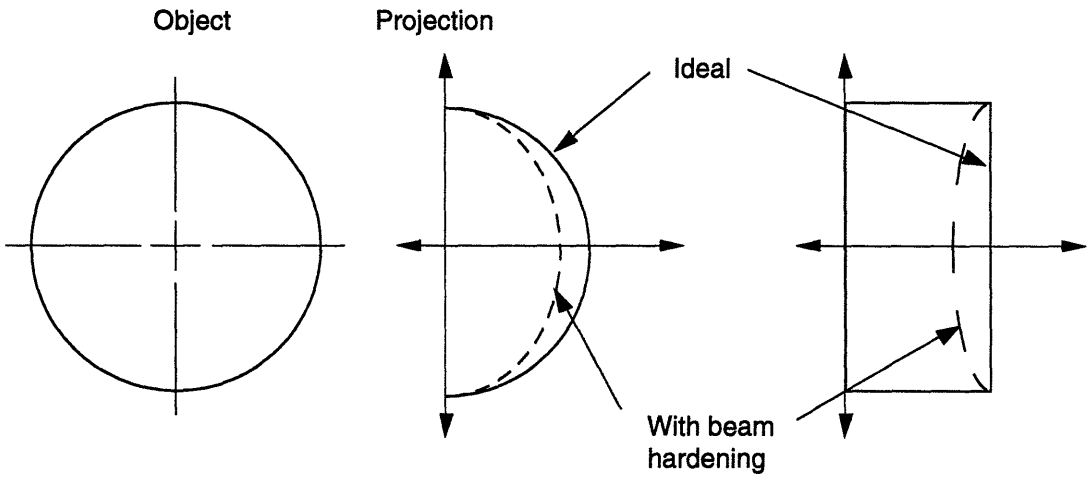

Figure 4.7 The effects of beam hardening (McFarland, 1994).

The effect of beam hardening can be reduced by adding x-ray beam filtration and normalizing the data with a cylinder object of similar size and material as the test object. In addition, beam hardening is often compensated for in the processing software. If the material being scanned is known, the measured transmission value can be empirically corrected even though there are difficulties when the object consists of several materials with widely varying effective atomic numbers. An iterative beam hardening correction,

i.e., processing technique for minimizing beam hardening artifacts, was implemented in the case in which the object is composed of two specific materials that are readily identifiable in the image (Joseph, 1978).

The finite number of the measurements, i.e., coarse sampling of detailed feature, can create falsely characterized data. The effect of this undersampling of the data is termed aliasing, in which high-frequency structures are recorded as low-frequency data. This effect can cause image artifacts that appears as a series of coarsely spaced waves or herringbone-type patterns over sections of the image. Aliasing can also occur as a result of the reconstruction process. If an image in which the pixel spacing is much greater than the finely sampled projection data, the high-frequency information in the projection data can cause aliasing artifacts in the image. This can be eliminated through appropriate selection of the reconstruction filter function to filter out or eliminate spatial frequencies higher than that contained in the reconstructed image matrix.

The Gibbs phenomenon is also a type of artifact associated with the limited spatial frequency response of the system. It is a consequence of a sharp frequency cutoff in the reconstruction filter function. This causes overshooting or oscillation along high-contrast boundaries. This type of artifact can be minimized by using a smooth roll-off reconstruction filter function rather than a sharp cutoff one at the high frequencies.

4.7 Shielding

In order to reduce the dose rate to an acceptable level at the position occupied by personnel, it is usually necessary to place barriers of lead, concrete, or some other material between them and the radiation source. A thick wall is installed to protect a radiation worker, non-radiation worker, and the public at large. The thickness of shielding necessary to reduce the exposure rate to an acceptable level depends on the output of the source, beam diameter, quantity of scattered radiation from the object and leakage radiation from the source housing, distance from the source to occupied areas, degree and nature of occupancy, shield material, and the type of installation. In making the calculations, it is essential to consider three types of radiation from the source: primary radiation, leakage radiation, and scattered radiation (American National Standard, 1993).

4.7.1 Primary shielding thickness

Primary radiation is the radiation from the source that emerges through the collimator. To calculate the required primary shielding thickness, it is only necessary to determine the desired value of the primary shielding transmission ratio, B_{pri}, and then find the corresponding thickness for the appropriate radio nuclide and the shield material of choice. The primary shielding transmission ratio, B_{pri}, is the ratio of the desired exposure rate outside the shield divided by the exposure rate at the same point without the shield present, and is defined as:

$$B_{pri} = \frac{PD_{pri}^2}{WUT}, \tag{4.8}$$

where P is the maximum permissible weekly exposure, D_{pri} the distance in meters from the source to the location in question, W (Workload) the weekly exposure in the useful beam, U the use factor or the fraction of the workload during which the useful beam is pointed in the direction under consideration, and T the occupancy factor or the fraction of the time during which a person is exposed. Its value depends on the desired exposure level that is used to maintain personnel exposures as low as reasonably achievable. From equation (4.8), the primary barrier thickness, X_{pri}, is obtained as:

$$X_{pri} = -\log\left(B_{pri}\right) \times TVL, \tag{4.9}$$

where TVL is the tenth-value layer of the shielding material. Smaller values of W, U, and T, or greater distances result in larger values of B_{pri} and therefore smaller thicknesses of shielding material.

4.7.2 Secondary shielding thickness

Secondary shields are exposed only to leakage radiation from the source and scattered radiation from the incident beam interaction with an object. Since these may be of considerably different energies, shielding requirements for leakage and scatter should be determined separately.

Leakage radiation from the source or target is always present. In a LINAC, radiation may be generated at a number of places along the beam transport system, but the main source is usually near the spot where the electrons are focused to produce the x-ray or at each bending magnet. There is no universal agreement on maximum permissible leakage levels. The International Commission on Radiological Protection (ICRP) and The U.S. National Committee on Radiation Protection (NCRP) have suggested that the leakage at 1 meter should be limited to 0.1 % of the useful beam. The barrier thickness based on the leakage radiation, X_{leak}, can calculated by:

$$X_{\text{leak}} = -\log(B_{\text{leak}}) \times TVL, \tag{4.10}$$

where B_{leak} is the leakage radiation transmission ratio, and it is defined as:

$$B_{\text{leak}} = \frac{PD_{\text{sec}}^2}{WUT} \times L, \tag{4.11}$$

where D_{sec} is the distance (in meters) between the scattering object and the area to be protected and L the percentage of leakage radiation from source housing.

Scattered radiation from the incident beam interacting with the object has a lower intensity and is usually of lower energy than the incident beam. Both the energy and intensity of the scattered radiation depend on the scattering angle, the energy of the primary beam, atomic number of the scatterer, and the scattering area (field size). Scatter calculations use two factors that describe the scattered radiation intensity. α is the ratio of scattered to incident radiation, which varies depending on energy and angle of scatter. A is the area of the radiation field at the scattering object. The calculation applies the inverse square relationship twice to account for the distance between source and scattering object, $D_{scatter}$, and the distance between the scattering object and area protected, D_{sec}. The transmission ratio for scattered radiation, B_{scatter}, is given by:

$$B_{\text{scatter}} = \frac{400PD_{\text{sec}}^2 D_{scatter}^2}{\alpha WTA}, \tag{4.12}$$

where 400 is the standardized area of the primary beam (in cm^2) at the scattering surface. The barrier thickness based on the scattered radiation, X_{scatter}, is also given by:

$$X_{\text{scatter}} = -\log(B_{\text{scatter}}) \times TVL. \tag{4.13}$$

As mentioned before, scattered and leakage radiation may be used to compute the secondary shielding thickness for each of the two separate effects. If the shield thicknesses computed separately are nearly equal (less than 3 HVL), then 1 HVL should be added to the larger single thickness to get the required total thickness. However, if one of the thickness is more than 3 HVL or greater than the other, the thicker one alone is adequate. The larger thickness permits transmission of the permissible level from one effect plus not more than one-eighth (3 HVL) of the permissible level from the other effect. This one-eighth excess is negligible in view of other conservative approximations involved.

For economic reasons, shields should usually be placed as near to the source as possible. Although the shield thickness is not reduced by this procedure, the area of the shield, thus the volume and weight are reduced. The shield weight is approximately proportional to the square of the distance between the source and the shield.

While concrete and similar materials generally provide the most economical shield, lead may be required where the space is limited.

CHAPTER 5

COMPONENT DESIGN AND APPLICATION OF TOMOGRAPHIC SYSTEM

Chapter 3 was established the technical background of CT with mathematical modeling and experiments, and Chapter 4 presented some design criteria and factors to be considered. In this chapter, these principles, insights, and experience gained from modeling and experimentation will be applied to the design of a real-time γ-ray tomographic imaging system for the continuous casting process.

5.1 Source Design

The choice of a radiation source is determined by the statistical variations in the count rate transmitted through the metal. Neglecting the forward scattering effect in equation (3.1), gamma ray attenuation is captured by the following exponential decay phenomenon with several easily measured physical parameters:

$$N = N_o \exp(-\lambda x), \tag{5.1}$$

where N is the number of photons transmitted, N_o the number of photons incident on the object being scanned, λ the linear attenuation coefficient of the metal, and x the beam path length. Consider the limiting case where the beam path length is the desired, spatial resolution of the image, Δx, is fixed for one set of experiments. Furthermore, under stable steady state experiment conditions, the incident photon count N_o is constant in macroscopic (but not in micro) time, so that the only remaining variation is the change in the attenuation coefficient $\Delta\lambda$. Taking the derivative of equation (5.1) yields a straight forward relationship between the change in the attenuation coefficient and the change in the number of photons passing through the material:

$$\Delta N = N_o \exp(-\lambda x)\Delta\lambda\Delta x = N\Delta\lambda\Delta x. \tag{5.2}$$

Since the linear coefficient is given by $\lambda = \mu\rho$, where μ is the mass attenuation coefficient (nearly invariant in the photon energy range used here) and ρ the density, equation (5.2) may be rewritten as:

$$\Delta N = N\mu\Delta\rho\Delta x \tag{5.3}$$

This ΔN is the desired signal, since it is directly correlated to the density variation $\Delta\rho$ which characterizes the phase change inside the material during solidification. At this point, N is not a deterministic number since the incident photon count N_o is governed by the quantum nature of electromagnetic radiation, whose model entails a probability distribution—namely Poisson distribution. From knowledge of Poisson distribution, the expected value of statistical variance from a measurement of N counts is $\sqrt{N}$. Hence, the order of the noise in the signal is roughly $\sqrt{N}$, and the signal-to-noise ratio (SNR) is :

$$\text{SNR} = \frac{\Delta N}{\sqrt{N}} = \sqrt{N}\mu\Delta\rho\Delta x \tag{5.4}$$

The SNR is a convenient measure of the quality of the signal or measurement, and is particularly important for a real-time measurement system, such as the proposed tomographic system. It is advisable to maximize the SNR subject to time and cost constraints. For the worst case scenario, let SNR = 1 to obtain the minimum photon counts required at the detector to produce an image with desired spatial and density change resolution by rewriting equation (5.4) as :

$$N = (\mu\Delta\rho\Delta x)^{-2} \tag{5.5}$$

Figure 5.1 depicts this relationship for a range of density change from 1 to 10 %, and the desired spatial resolution from 1 to 10 mm for 203.2 mm thick iron, whose density is 7870 kg/m^3 and mass attenuation coefficient is 3 mm^2/g. The qualitative explanation of the graphs agrees with physical intuition: smaller density change or finer spatial resolution is more difficult to detect and image, and therefore requires more measurements, which would translate to larger photon counts at the detector and thus longer measurement time. To make this patently clear, three distinct cases can be compared: to image 1 % density change with 4 mm spatial resolution, nearly 10^6 photons need to be counted at the detector, compared with only 3×10^5 photons if the density change were increased to 2 %, or if the spatial resolution is increased to 8 mm.

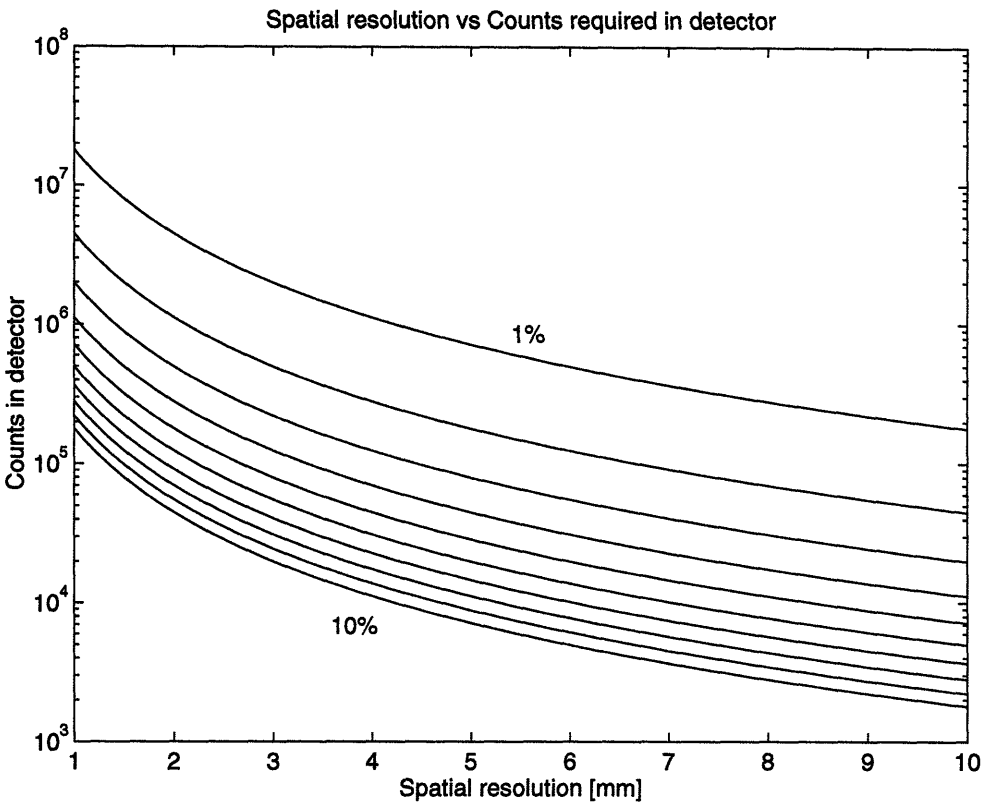

Figure 5.1 System performance graph of spatial resolution versus counts required in detector.

Associated with the photon counts is the photon flux at detector Φ_{det} which is the photon counts per unit area, hence it follows the same trend as N, as shown in Figure 5.3. In this case, the area refers to the area of the surface normal to the incident radiation beam path, as shown in Figure 5.2 with an incremental volume of the object being scanned. The area subject to radiation, A, is $\Delta y \Delta z$, and the flux at detector Φ_{det} is accordingly:

$$\Phi_{det} = \frac{N}{A} = \frac{1}{\mu\rho\left(\frac{\Delta\rho}{\rho}\right)^2 \Delta x^2 \Delta y \Delta z} \tag{5.6}$$

Motivated by the experimental procedures described in Chapter 3, where the vertical step size is the image slice thickness, Δz is taken to be 10 mm, a typical value for slice thickness. Furthermore, since Δx and Δy measure dimensions on the same plane, and the plane is scanned from all directions, there is nothing intrinsic in the orientation of the axes,

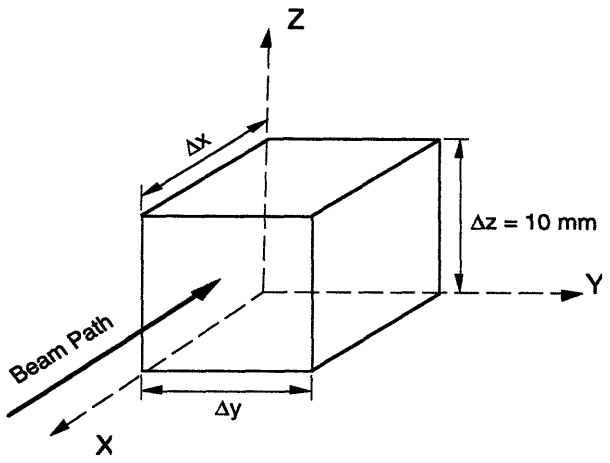

Figure 5.2 Schematic of voxel image.

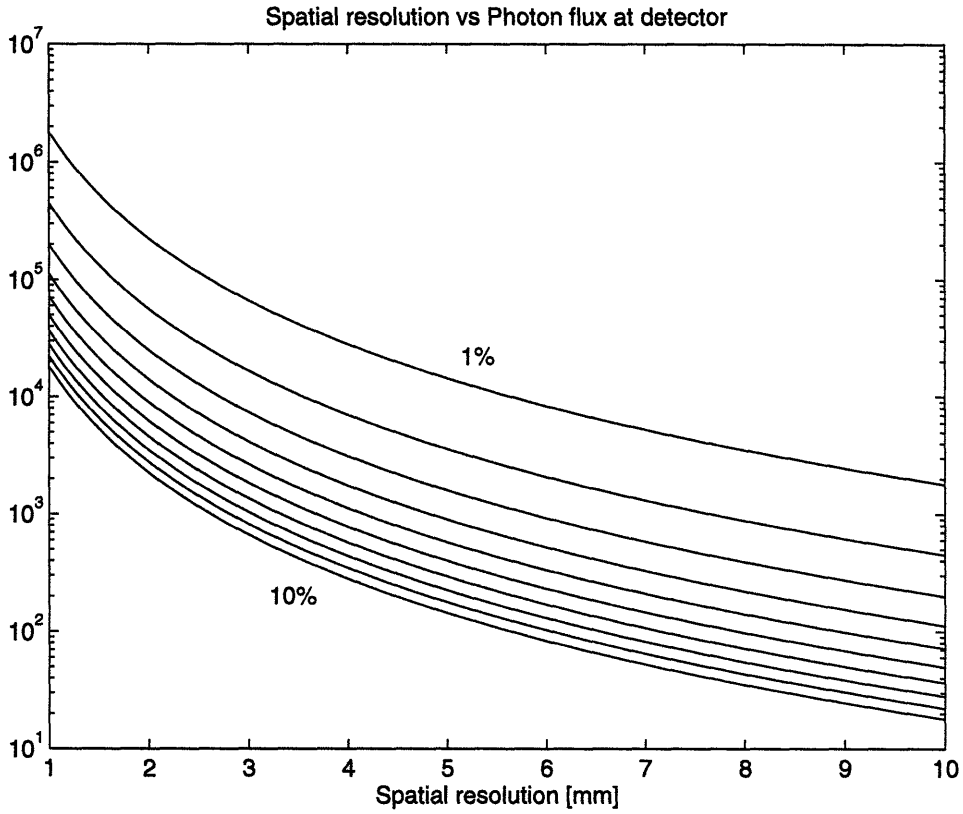

Figure 5.3 System performance of spatial resolution versus photon flux at detector.

which obviate the need to differentiate Δx and Δy. Instead, one generic variable Δ may be used to represent the spatial resolution of the two-dimensional slice image. Using this simplified variable Δ, equation (5.6) can be rewritten as:

$$\Phi_{det} = \frac{1}{\mu\rho\left(\frac{\Delta\rho}{\rho}\right)^2 \Delta^3 \Delta z} \tag{5.7}$$

Figure 5.3 relates the required photon flux at detector to achieve a given spatial resolution with the various density changes.

Intuitively, the larger the flux, the stronger the radiation strength. Ultimately, the strength and the characteristics of photon beams are controlled by the radiation source. In the literature, the source strength is indicated by its dosage, which is by definition energy deposited per unit mass and can be translated to the energy of the radiation at some fixed distance from a unit mass of the source material per unit time. Hence, the unit of dosage is $\mathrm{MeV/(g \cdot s)}$, or simply rad/s for convenience, where 1 rad/s = 6.25×10^7 $\mathrm{MeV/(g \cdot s)}$ by definition. In practice, the dosage is not measured directly, but derived from the source flux at a given distance, times the mass attenuation coefficient, which accounts for the radiation absorption property of the source, i.e.:

$$\text{dose} = \mu_{src} \Phi_{src} \tag{5.8}$$

A high energy accelerator such as a LINAC does not provide monoenergetic radiation as dose radioisotopes. It has instead an energy spectrum ranging from E_{min} to E_{max}. Although a photon from the source may be at any energy within the spectrum, an average of the energy spectrum can be used to approximate the photon energy. The average energy of a photon from a source with an energy spectrum ranging from E_{min} to E_{max} is:

$$E_{ave} = \frac{E_{max} - E_{min}}{\ln(E_{max}/E_{min})} \tag{5.9}$$

For example, if E_{max} is 6 MeV and E_{min} is 1 MeV, then E_{ave} is 2.71 MeV. According to equation (5.9), which implies how much energy each photon has, the source flux can be converted to how many photons are generated per each second as:

$$N_{inc} = \Phi_{src} E_{ave} \tag{5.10}$$

The photon count at detector in Figure 5.3 is the incident photon count at the object attenuated while passing through the object, as described by equation (5.1). Finally, by combining equation (5.1) and (5.10), N_{det} can be obtained as:

$$N_{det} = \frac{2.08\times10^{9} X(\text{Rad}) \ln(E_{max}/E_{min}) \exp(-\mu\rho D)}{E_{max} - E_{min}} \tag{5.11}$$

In fact, this calculation can be repeated for ranges of dosage and the source energy spectrum. While it is difficult and impractical to characterize the energy spectra of various sources, their respective average energies conform more or less to equation (5.11). Furthermore, if the minimum energy were assumed to be 1 MeV, it makes the comparison of the sources even simpler. Figure 5.4 shows the linear dependence of the output flux on the dosage for sources with E_{max} of 3, 6, 9, 12, and 15 MeV, respectively. According to the graph, E_{max} and the photon flux have a qualitatively complementary relationship, that is, increasing one decreases the other. For example, a 15 rad source can emit only 5×10^{5} photons/$(\text{mm}^2 \cdot \text{s})$ if E_{max} = 15 MeV, compared with 7×10^{5} photons/$(\text{mm}^2 \cdot \text{s})$ if E_{max} = 9 MeV.

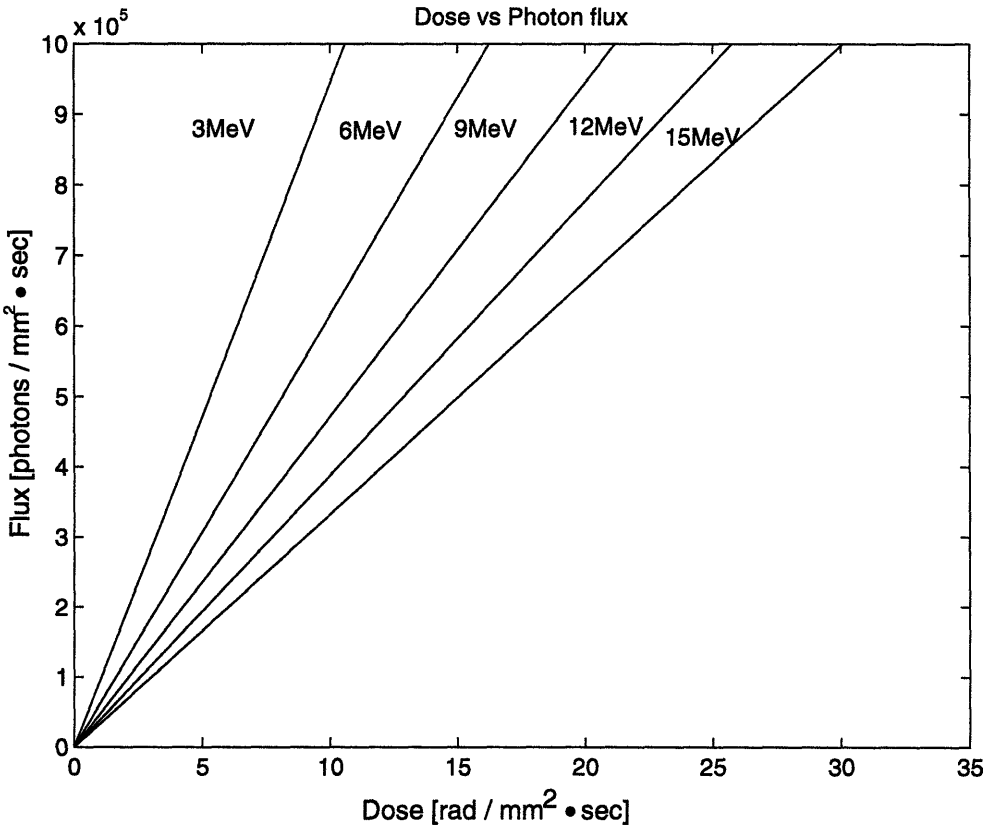

Figure 5.4 System performance graph of source strength versus photon flux.

5.2 Detector Design

Radiation from the source passes through the source beam collimator and is then attenuated while passing through the object being scanned. Chapter 3 discussed how the information leading to interior density of the object being scanned can be extracted from this radiation attenuation. Therefore, the radiation emerging from the object and arriving at the detector is far more than just radiation; it is the desired information. It is up to the detector to retrieve the embedded information quickly and accurately. This section presents some fundamental considerations that affect detector performance.

5.2.1 Detector efficiency

Chapter 4 discussed the fundamentals of the scintillation detectors used in the present designs. Of the many traits that characterize a detector, efficiency is one of the top priorities for use in an integrated tomography environment. This section presents a valid working model of the scintillation crystal detector efficiency that can be used to facilitate the system design.

Scintillation detectors produce measurement signals when energetic photons are absorbed into its crystal in which some incident photons are absorbed in the crystal of thickness l_d, and some pass through. The likelihood of absorption (note that this analysis stems from the probabilistic approach due to quantum nature of radiation) is directly dependent on the energy spectrum of the photon source matched to the absorption spectrum of the detector crystal and the geometry of the crystal panel. This situation is in accord with the premises in the previous section, in which photons being absorbed into the object being scanned obeyed the exponential decay relationship given in equation (5.1). The efficiency, η, is now related to the percentage of the absorbed photons to the total incident photons, or the percentage of the photons *not* passing through the crystal to the total, i.e., if the number of incident photons is N_o:

$$\eta = \frac{N_o - N_o \exp(-\lambda l_d)}{N_o} = 1 - \exp(-\lambda l_d) \tag{5.12}$$

where λ is the linear attenuation coefficient of the detector crystal and l_d the crystal thickness. To characterize the detector efficiency, it only remains to look up the values of the linear attenuation coefficient, or alternatively, mass attenuation coefficient, in the range of source strength. But even without concrete values, it is obvious that increased crystal thickness improves the efficiency monotonically, consistent with physical intuition. Indeed, this reflects in the cost of the crystal; thicker crystals are disproportionately more expensive than thinner ones. Figure 5.5 shows in the 100 keV to 10 MeV photon energy range the theoretical detector efficiency of a $CdWO_4$ detector crystal, which is most suitable for a high energy source. Since the operating energy range of the current approach is above 4 MeV, the maximum theoretical detector efficiency can be expected to be slightly below 60 % for the 32 mm thick crystal. As will be elucidated in the following section, the required exposure time is inversely proportional to the detector efficiency because only some of the photons hitting the detector are registered and converted into a useful, measurable signal. Once again, this requires a careful compromise between the allotted budget and other factors including sensor speed, prolonged radiation exposure risk, and image quality.

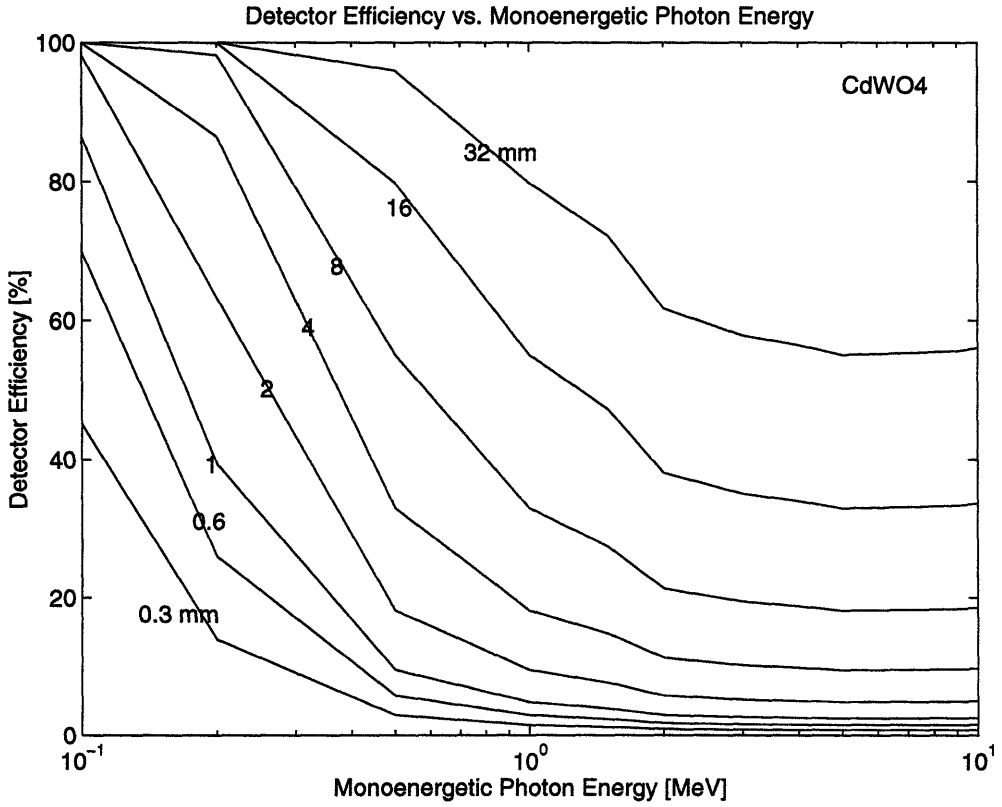

Figure 5.5 Theoretical detector efficiency.

5.2.2 Dynamic range

Dynamic range is the range of useful signal to the detector. Radiation intensity below the minimum measurable level is noise. On the other hand, excessive radiation saturates the detector and cannot be measured. This requires detector be tuned to the expected radiation intensity at the detector. As mentioned in the section 4.2.1, the dynamic range is usually specified as a ratio of the maximum signal output to the minimum. The maximum signal is, of course, the incident photon count N_o and the minimum signal can be calculated in equation (5.2), i.e., the photon variations passing through the material, as given by:

$$\Delta N = N_o \exp(-\lambda x)\Delta\lambda\Delta x = N_o \exp(-\lambda x)\mu\Delta\rho\Delta x. \tag{5.13}$$

Thus, the dynamic range can be calculated as:

$$\mathrm{DR} = \frac{N_o}{N_o \exp(-\lambda x)\mu\Delta\rho\Delta x}. \tag{5.14}$$

For instance, to detect a 1 % density change and 1 mm special resolution for an ideal case, a dynamic range of 5.2×10^5 is needed.

5.2.3 Detection angle analysis

The central point for all the discussions so far is the radiation attenuation phenomenon expressed by equation (3.1) in which forward scattering is neglected. Unfortunately, as stated in Chapter 4, the dominant mode of photon-electron interaction in the range of photon energy used for the current setup is Compton interaction, which is especially prone to scattering than other modes. Scattered radiation therefore becomes even more important, and the assumption of negligible forward scattering must be tested rigorously. Forward scattered radiation increases the photon counts at the detector, distorting the true density change inside the caster. Needless to say, it is beneficial for accurate measurements to minimize this forward scattering effect, despite the qualitatively predictable nature of the perturbation cased by forward scattering. At present, this is

implemented with an anti-scatter collimator mounted in front of the detector crystals, as shown in Figure 5.6

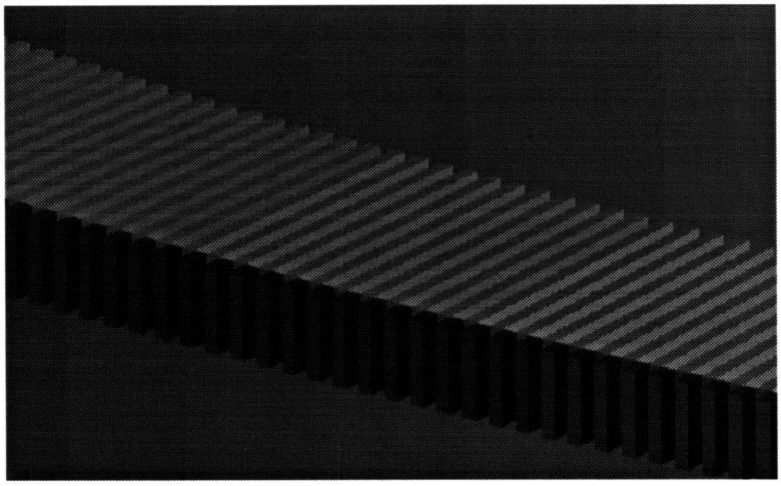

Figure 5.6 Three-dimensional rendering of an anti-scatter collimator configuration.

Ideally, the photon through the caster should hit the detector crystal head-on, in which case the incident beam angle θ is zero according to the above figure. Even if the photon does not approach the detector at a perfectly normal angle, the finite length and thickness of the anti-scatter plates in the collimator allow the photon to avoid the anti-scatter plates altogether—up to a point. Beyond that, the photon will go through the plate, emerge to the ambient air, and then hit the detector at the same angle θ. Obviously, the simpler case analyzed in Section 5.2.1 is a special case of this more general situation, and even before the model for a more general setup, the end results for the two cases are expected to be congruent. With that explicit condition stated, it becomes possible to model the detector-collimator efficiency.

The anti-scatter plates in the collimator are passive elements that merely attenuate the radiation, and introduce no new physics to the phenomenon for an extreme case, as discussed in Section 5.2.1, so that the beam path length through the detector crystal controls the theoretical detector efficiency. However, since the incident beam may have been attenuated through the collimator, the overall efficiency is decreased by the fraction of the photons surviving through the collimator. In fact, the sole function of the anti-scatter plates is the attenuation of radiation approaching the detector crystals at an angle oblique to normal of the detector crystal surface, therefore allowing only those photons deviating from the normal by a sufficiently small angle to be considered as having passed through the object. For maximum attenuation, high density material is preferred. The current design

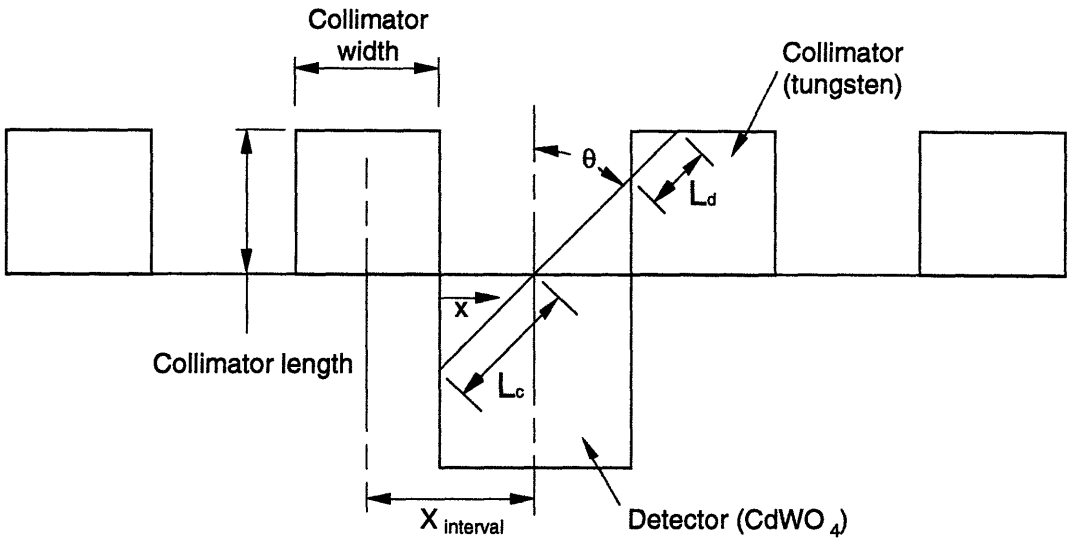

Figure 5.7 Schematic of collimatior and detector set-up.

employs $CdWO_4$ for the detector crystal and tungsten, whose density is 0.193 g/mm^2, more than twice that of steel, for the collimator. Putting the two terms together:

$$\eta = \exp(-\lambda_c L_c)\left[1 - \exp(-\lambda_d L_d)\right] \tag{5.15}$$

where λ_c and λ_d are the linear attenuation coefficients of the collimator and detector materials, respectively, and L_c and L_d are the beam path lengths through the collimator and detector crystals, as shown in Figure 5.7. Since the path lengths through each material are functions of their geometry and the incident beam angle θ, a family of curves relating the detector efficiency to the beam incident angle can be plotted for a range of collimator and detector crystal geometries. Intuitively, the longer the collimator relative to the detector crystal is, the more insensitive the detector will be to off the normal radiation beams, and consequently, to forward scattered radiation. Figure 5.8 generated from a numerical computation (Jureidini, 1996) programmed in IDL data analysis software assuming 100 collimators on each side confirms this trend with sharper and narrower central peaks as each parameter of the collimator is changed.

The implications of longer and wider collimator plates, as well as thicker detector crystals are clear and direct. As an example, Figure 5.8 (a) shows the detector efficiency improvement as the crystal thickness is increased from 3 to 25 mm. While the absolute amount of off-angle scattering effect remains the same, the thicker crystal and consequently higher conversion efficiency at the normal angle reduces the relative scattering effect.

Figure 5.8 (b) shows the result of thickening the collimator plates from 0.5 to 2 mm. The first order effect is the overall drop in detector efficiency due to the now smaller crystal

dotted line : Detector width: 1.5 mm, fixed
Crystal Thickness: 3 mm
Collimator width: 0.5 mm
Collimator length: 40 mm

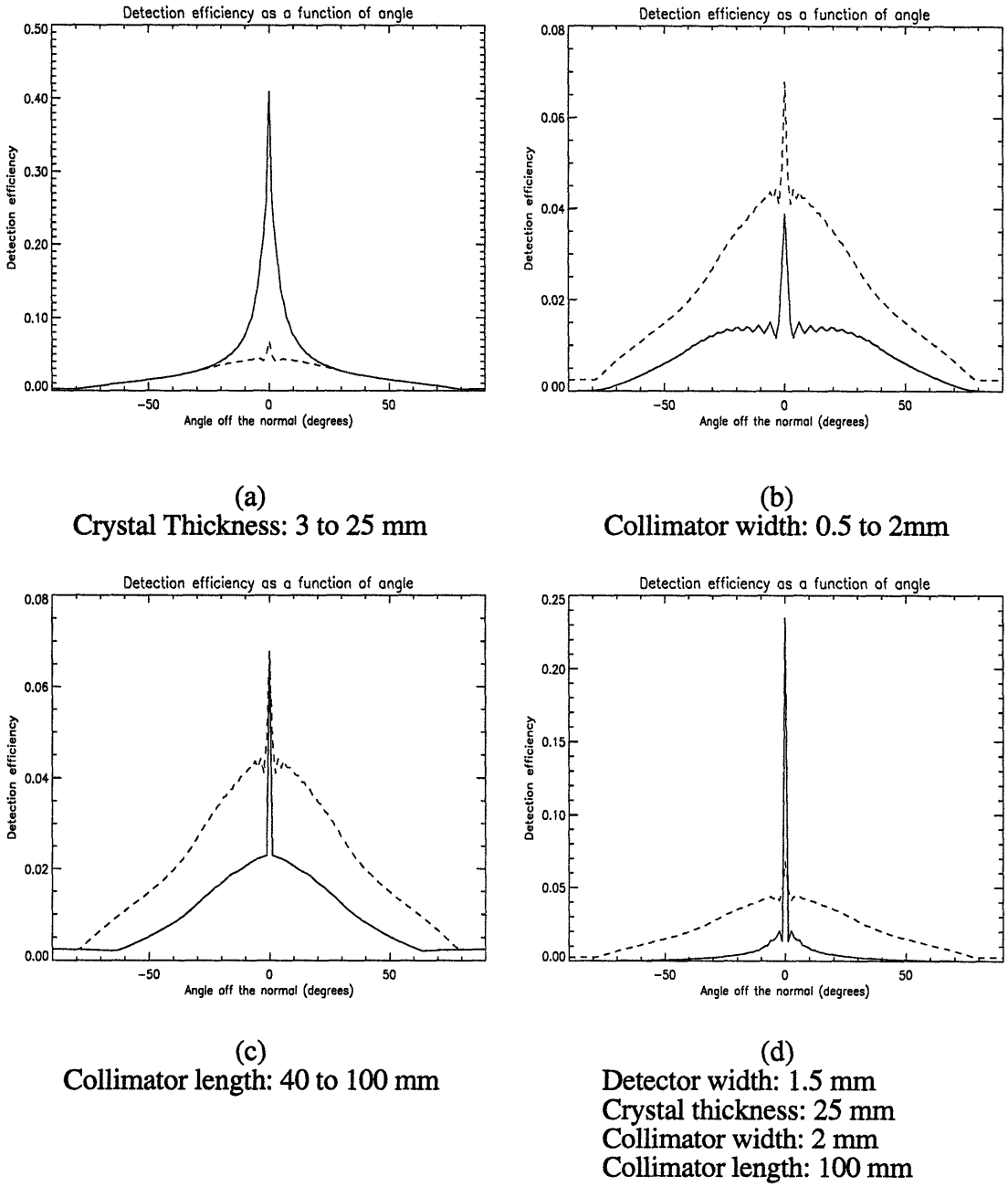

(a)
Crystal Thickness: 3 to 25 mm

(b)
Collimator width: 0.5 to 2mm

(c)
Collimator length: 40 to 100 mm

(d)
Detector width: 1.5 mm
Crystal thickness: 25 mm
Collimator width: 2 mm
Collimator length: 100 mm

Figure 5.8 Detection efficiency as a function of angle with various changes of geometric parameter.

surface relative to the collimator plates The scatter radiation drops along with overall detector efficiency. Figure 5.8 (c) is the comparison of the efficiency as the collimator plate length is increased from 40 to 100 mm. At precisely the normal angle, the surface area of the detector crystal that is exposed to the incident radiation is independent of the collimator length, so that the efficiency at this angle is unchanged.

For a non-zero approach angle, however, the attenuation is more severe due to a longer beam path length through the collimator plates. This is clear from the trigonometric relationship of the beam path length through the collimator to the collimator length, as shown in Figure 5.7. This is the most effective solution of the three independent parameter variations considered so far. Finally, when the three cases are combined, a dramatic improvement in scatter radiation rejection and detector efficiency for normal angle radiation is evident from Figure 5.8 (d). In the limit where the collimator length and the crystal thickness approach infinity with all other dimensions remaining constant, the efficiency curve approaches the Kronecker delta function of θ, $\delta(\theta)$, which is the preferred profile based on the original motivation for the collimator. However, the message from Figure 5.8 (a) through 5.8 (d) is not to spend all the allotted budget in making the central peak sharper; rather, it presents several design options for making a cost-effective detector to meet the specified scatter radiation rejection for different system optimization requirements.

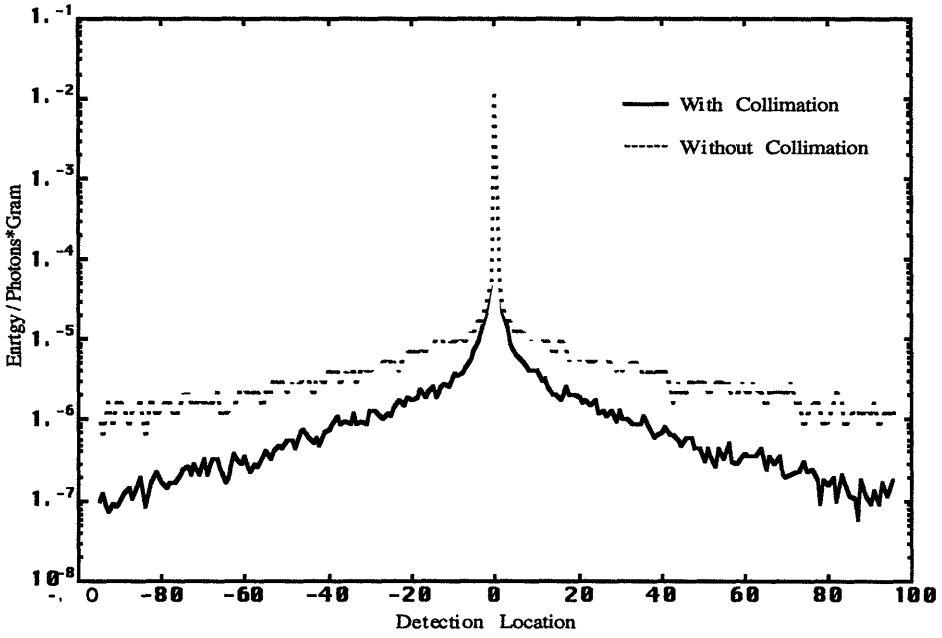

Figure 5.9 Comparison of point spread function between a collimated and uncollimated set-up.

Applying the design rules established above to the present experimental setup, a simulation of the detector performance was run using Monte Carlo N-Particle Transport Code system (MCNP). The simulation results, shown in Figure 5.9, confirm the design rules.

5.3 Exposure Time

Scanning speed, which is important in most applications, is constrained by the need for enough photons so that their statistical noise does not exceed the density differences being measured. The more photons are collected, the better the SNR; hence slower scans result in better density discrimination. To estimate scanning time, the number of photons per second through the thickest part of the object should be calculated, and then multiplication of this by the number of measurement positions necessary to traverse the scanning distance should followed. In digital radiography, this will be the dimension of object divided by the resolution in the scanning direction. In computed tomography, the situation is more complicated, but a first approximation is the circumference of the object divided by the resolution.

The time to detect and measure precisely the path length in a liquid metal depends on the source strength, the sensitivity of the penetration detector or detectors, and on the total path length through the metal and ancillary metal components and structures of the continuous casting apparatus. For example, the total attenuation of a radiation beam may be substantial and may therefore require an unreasonably large radioactive source. For this reason, the use of non-radioisotope radiation sources may be necessary for large casting systems, particularly for dense materials such as steels. Also, the attenuation coefficient for most materials is still declining at energies characteristic of Co^{60} gamma rays and does not exhibit the desired elemental independence until 2 to 3 MeV energies. Electronic sources such as LINACs are the equivalent to impractically large Co^{60} sources and have the further advantage of an off switch. Such machines are commercially available and provide a substantial increase in flux at higher energies. The actual time for a complete tomographic image will depend on the total number of measurements to be made to obtain the desired information, such as spatial resolution and scanning area. Also, since an accelerator such as a LINAC has higher energy and intensity, it allows the beams to pass through the support structure surrounding the metal, so that the sensor can be positioned more conveniently in the typically crowded area around industrial casters.

the required source strength corresponding to performance specification may be inferred from the criteria described in Section 5.1. Along with the source strength, the exposure time is an especially critical issue in the tomographic sensor design given that the sensor must be operated on-line, as well as safely. In order to produce a standard criterion for exposure time, a practical example based on a 6 MeV strong MINAC 6 used for the lab setting is given here. The output radiation of source MINAC 6 is rated at 5 rad/s @ 1m, or 3.13×10^8 MeV/g @ 1m where 1 rad = 6.25×10^7 MeV/g. From equation (5.8), the average energy of a photon from a source with energy spectrum ranging from E_{min} = 1 MeV to E_{max} = 6 MeV is approximated as E_{ave} = 2.71 MeV. If each photon has E_{ave} on the average, then dosage indicates the expected number of incident photons at some fixed distance from a unit mass of the source per unit time. For our source at hand, dose = 3.13×10^8 MeV/(g·s) @ 1m* 1 photon/2.71 MeV = 1.12×10^8 photons/(g·s) @ 1m. As mentioned in Section 5.1, the dosage is not measured directly, but derived from the source flux at a given distance, times the mass attenuation coefficient, which accounts for the radiation absorption property of the source, i.e.:

$$\text{dose} = \mu_{src}\Phi_{src} \tag{5.8}$$

On the other hand, for this MINAC 6 system, the dosage is already specified by the manufacturer. By rewriting equation (5.8), the source flux is then:

$$\begin{aligned}\Phi_{src} = \frac{\text{dose}}{\mu_{src}} &= \frac{1.12\times10^8\left(\dfrac{\text{photons}}{\text{g}\cdot\text{s}}\ @\ 1\text{ m}\right)}{3\left(\dfrac{\text{mm}^2}{\text{g}}\right)} \\ &= 3.73\times10^7\left(\frac{\text{photons}}{\text{mm}^2\cdot\text{s}}\ @\ 1\text{ m}\right)\end{aligned} \tag{5.16}$$

Now, the photon flux at detector Φ_{det} is simply the photon counts per unit area given in equation (5.6). Taking the exponential radiation attenuation as much as the object thickness into account, the required incident flux at the object is therefore given by:

$$\Phi_{inc} = \frac{(\text{SNR})^2\exp(\mu\rho D)}{\mu^2\Delta\rho^2\Delta^3\Delta z}. \tag{5.17}$$

It is critical to note the difference between the source flux Φ_{src} and the incident flux Φ_{inc} at the object being scanned. In fact, even their units are different; Φ_{src} represents the instantaneous number of photons generated from the source and passing through a unit area at a given distance, and Φ_{inc} represents the total accumulated number of photons incident at, i.e. that have reached, the object. If extraneous radiation incident at the object is negligible compared with the radiation from the main source and assuming that all the radiation incident at the object comes from the source, Φ_{inc} is the time integral of Φ_{src} and is given by:

$$\Phi_{inc} = \int \Phi_{src} dt \,. \tag{5.18}$$

Since the linear accelerator has a constant flux, equation (5.18) simplifies to:

$$\Phi_{inc} = \Phi_{src} t_{req} \,, \tag{5.19}$$

where t_{req} is the exposure time required for one measurement. Thus:

$$t_{req} = \frac{\Phi_{inc}}{\Phi_{src}} = \frac{(\mathrm{SNR})^2 \exp(\mu\rho D)}{\mu^2 \Delta\rho^2 \Delta^3 \Delta z} \cdot \frac{1}{\Phi_{src}} \tag{5.20}$$

As can be seen in equation (5.20), the higher the SNR, the longer the time required. While the exposure time is a power function of the SNR, density change $\Delta\rho$, and spatial resolution Δ, it is an exponential function of the object size D, so that the maximum object size more than anything drives the design. Of course, due to the finite efficiency of the detector, not all photons arriving at the detector will be converted to useful signals. In fact, all these processes are serial, so that the ideal exposure time in equation (5.20) must be divided by the product of the detector signal conversion efficiency and the geometric efficiency to yield the actual required exposure time. Thus, the total exposure time is defined as:

$$t_{tot} = \frac{t_{req}}{\eta_{det} \eta_{geo}} \,. \tag{5.21}$$

where η_{det} is the detector signal conversion efficiency and η_{geo} the geometric efficiency.

If the resulting time is unacceptably long, then the design process must be reiterated with necessary improvements and/or compromises. Some possible solutions are:

- If there is no penalty in spot size, a higher voltage source will have more photons per mA and better penetrating photons.
- If possible, use deeper, more efficient detectors, or add more detectors by filling any gaps between them, or by using a wider array in second generation CT systems.
- If x-y resolution in CT is of primary concern, increase the slice thickness.

5.4 Tomography System

5.4.1 Practical real time imaging techniques

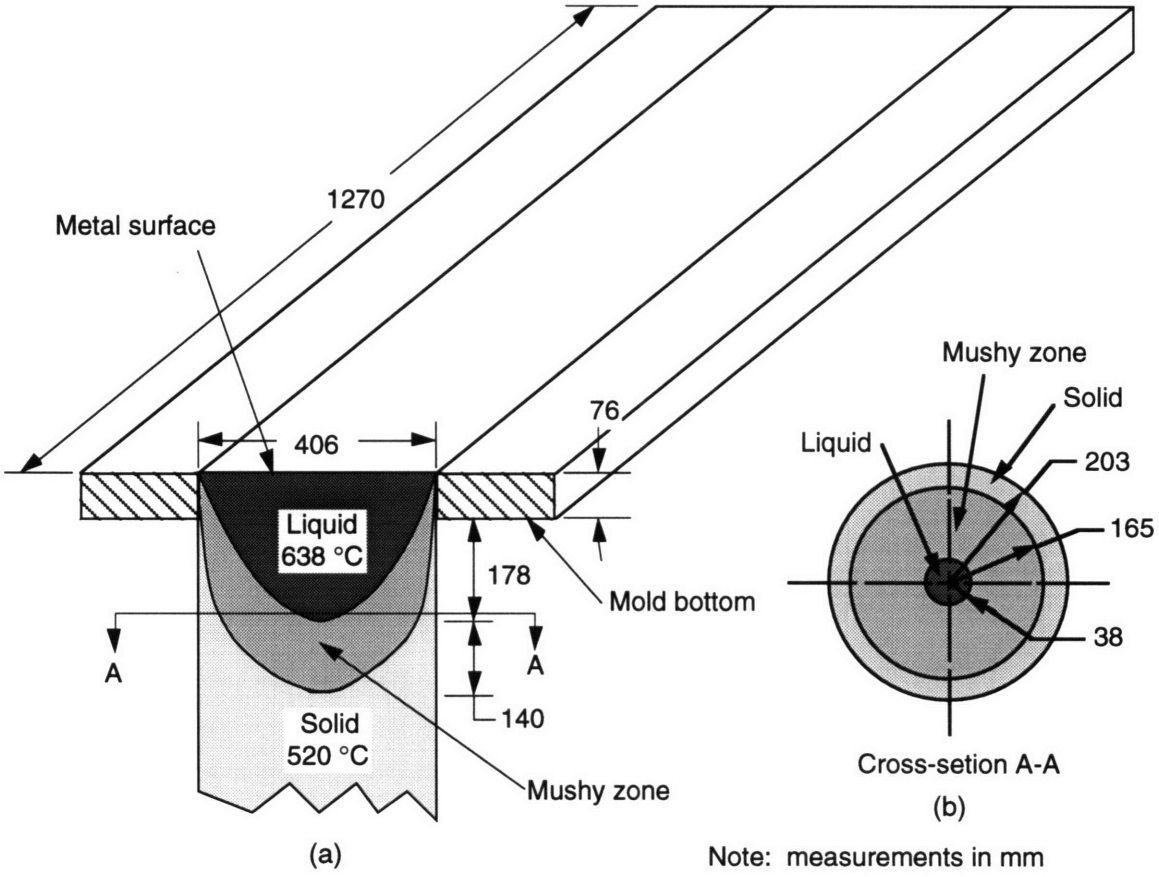

Figure 5.10 Schematic of a target caster.

Through the above discussions, the conceptual basis and feasibility of the computed tomography method for non-invasive monitoring of the continuous casting process have been firmly established. Still, the image acquisition time and the final image resolution are some of the issues to be resolved before this technique can become commercially attractive. These problems are formidable, given the huge size of industrial casters and the high throughput required for efficient operation. For example, the target caster shown in Figure 5.10 for future installation measures 1.27 m in length for the mold alone, let alone all other peripheral equipments such as the heating and cooling unit and insulation.

In fact, the aluminum in the core of the mold is only 406 mm wide. Since rearranging the existing fixed equipment layout or operation procedure is impossible in practical, it follows that the object must remain stationary, while the source and the detector must move around the existing caster. This is in contrast to the preliminary feasibility investigation conducted at MIT, in which the source and the detector were held stationary while the object in the middle was rotated and translated. Nevertheless, the fundamental technique and issues are invariant.

In addition to the difficulty with having to actuate and synchronize the source and the detector, the huge size of the "object" to be scanned presents herculean technical challenges. Wasting the finite beam intensity of the source and the finite area, and already poor overall efficiency of the detector to image existing peripheral equipments is undesirable when the point of interest is only the core of the mold where the metal solidification process is taking place. Unfortunately, this is unavoidable under the present circumstances, because the computed tomography method necessitates the measurement of *all* objects in between the source and the detector. Instead, some improvements can be made in the imaging process after detector measurements are made by taking advantage of the invariance of all ancillary equipments surrounding the solidifying metal, including the mold. This is helpful in shortening the continuous image processing time for real-time monitoring. Essentially, the idea is to take the difference of the actual measurements from the predetermined measurements taken when the caster is empty, or full of solid metal—whichever is a convenient reference—so that all images of materials between the source and the detector other than that of the solidifying metal are canceled out and the post processed image contains only the section of interest, as shown in Figure 5.11.

The graph shows the result of applying the above algorithm to a simulation using IDL. The desired core image of aluminum in the caster was obtained by subtracting the reference image from the original image obtained with normal tomographic imaging. The graph shows conclusively that existing tomographic reconstruction algorithm is unaffected by the simplification technique outlined above.

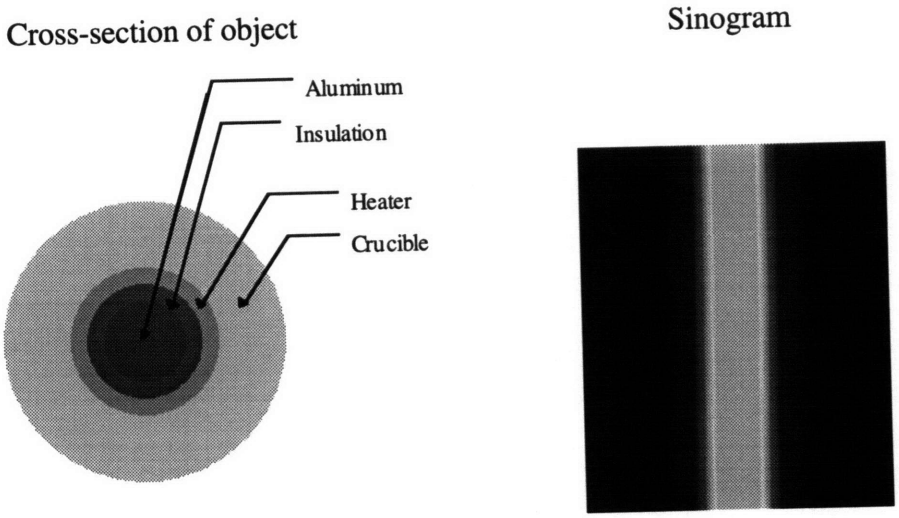

(a) Object with full solid aluminum in the crucible

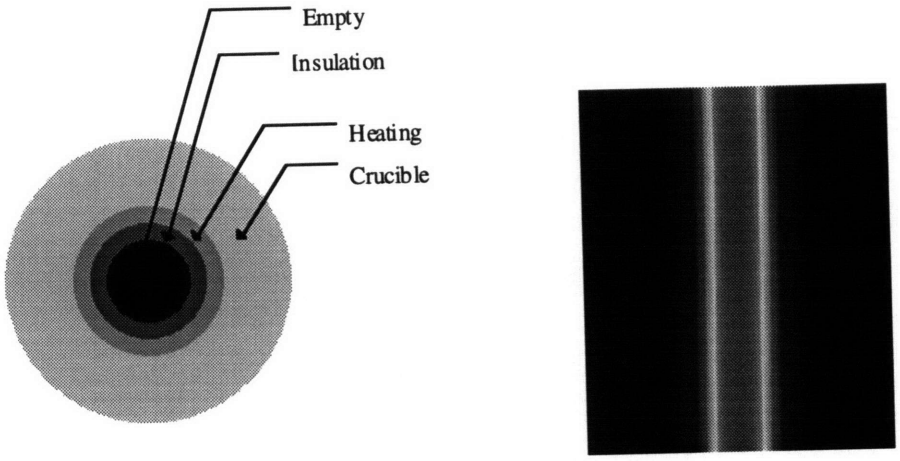

(b) Object with no aluminum in the crucible

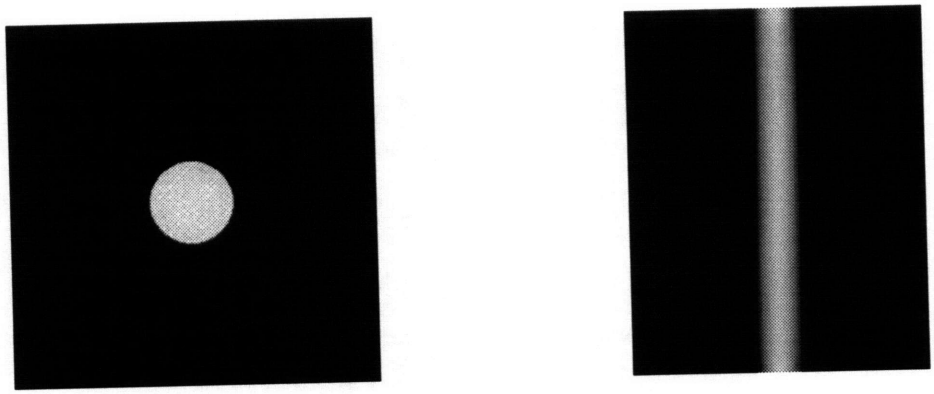

(c) Filtered backprojection of the difference

Figure 5.11 Example of practical real-time imaging technique.

5.4.2 Mushy zone analysis through tomography

Mushy zone is the layer between the molten and solidified metal in which the actual solidification process takes place. Mushy zone characterization has far reaching implications for both academic and practical purposes, because critical parameters for casting processes such as impurity inclusion, defect growth, and heat transfer are controlled by the dynamics of what goes on inside the mushy zone. Consequently, geometrical characterization is one of the major goals of the project. New challenge lies in an effective incorporation of existing tomography techniques, which are geared toward imaging objects with the sharp boundary rather than gradual continuous density change taking place within the solidification front. For this reason, mushy zone characterization is an especially meaningful watershed for the project.

Having established the motivation for the mushy zone study, the considerations and appropriate steps in accomplishing the goal will be described, which will also aid the understanding of the general tomography principle. The starting point of the discussion is the cross section A-A of the solidification region in the target caster setting shown in Figure 5.10. The solid/liquid distribution of the cross section is shown in Figure 5.10 (b).

Since the spatial resolution must be sufficiently fine to capture the gradual density change across the mushy zone, several performance requirements on the tomography system, such as the minimum linear and angular steps taken during scanning, should be met.

Figure 5.12 shows the profile of the density corresponding to the solidification region A-A shown in Figure 5.10. The region of interest was assumed for the ideal gradual density change. For aluminum, the densities of liquid and solid states are 2400 kg/m^3 to 2700 kg/m^3, or approximately 12 % increase. This density variation appears as a thin annulus in the tomographic image. When many such layers are superimposed to form a three-dimensional image, the geometry of the mushy zone can be established. The quality of the image is controlled by the spatial and density change resolution of the system, which in turn is decided by the number of measurements taken for one image. For example, if the 12 % density change is to be viewed with 0.1 % resolution in the 127 mm wide mushy zone, the spatial resolution Δ must be at least 1.06 mm. Since the interior diameter of the mold L is 406.4 mm and the number of sampling should be at least twice according to the Nyquist theorem, then the number of projection required for the desired spatial resolution, N_s, is:

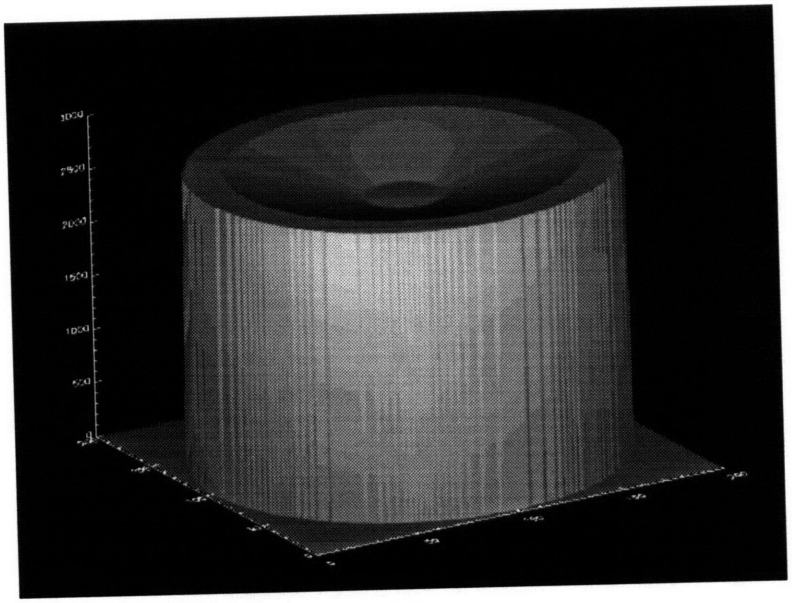

(a)

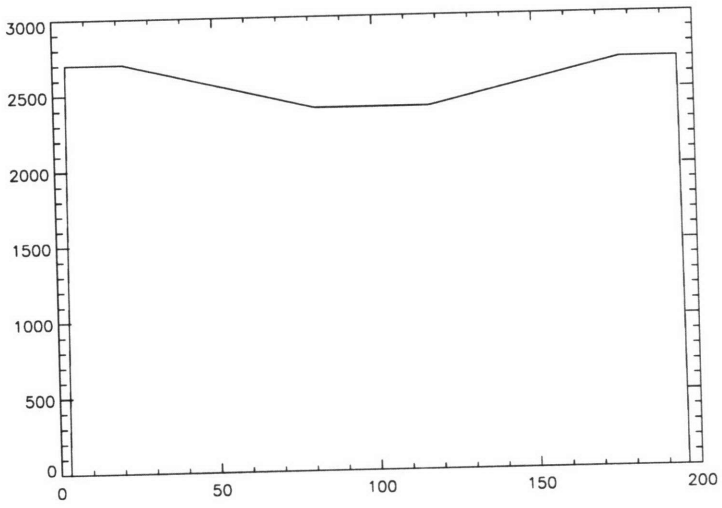

(b)

Figure 5.12 Density map of the region A-A: (a) three dimensional density profile, (b) the density profile of one projection.

$$N_s = 2 \times \frac{L}{\Delta} = 2 \times \frac{406.4}{1.06} = 767. \tag{5.22}$$

And the lower bound on the number of angular steps is proportional to the number of translational movements by the constant scalar factor of $\pi/2$, and is given by:

$$N_\theta \geq \frac{\pi}{2} N_s \,. \tag{5.23}$$

Thus the number of angular steps on the actuator is $N_\theta \geq 1205$.

Once the data are collected for all values of N_s and N_θ, the data are gathered to form a two-dimensional representation called "sinogram" such as those shown in Figure 5.13, which is the input data and can be used to check the centering before inputting the data into the reconstruction process.

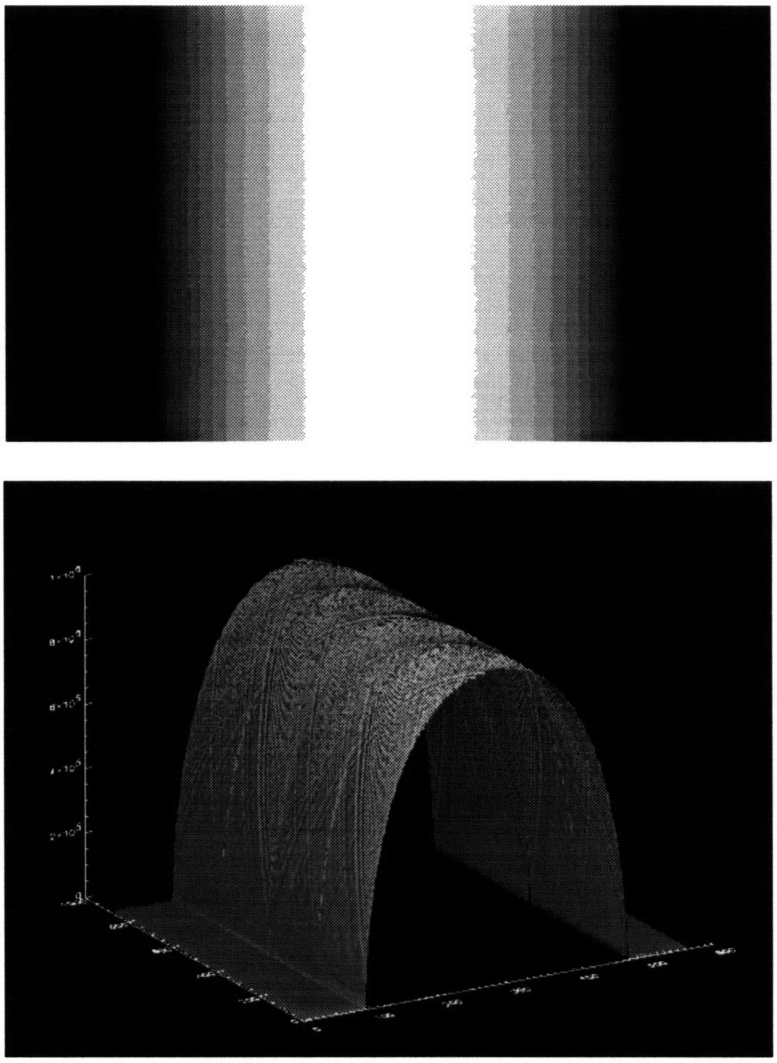

Figure 5.13 Sinograms of the object.

By filtering this projected data through a reconstruction algorithm, a three-dimensional density profile such as the one shown in Figure 5.14 can be established. In a real application, the reconstructed image is formed based on the radiation attenuation measurements discussed in previous chapters. However, Figure 5.14 was constructed

from an alternative data generated by integrating the beam path length through a simulated object programmed in IDL (Jureidini, 1996).

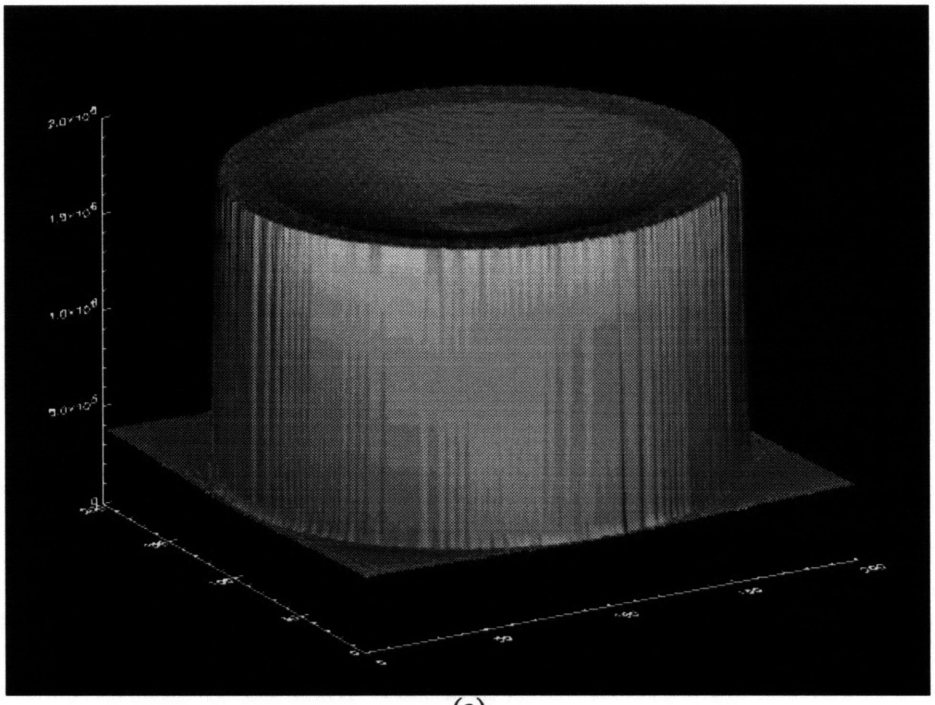

(a)

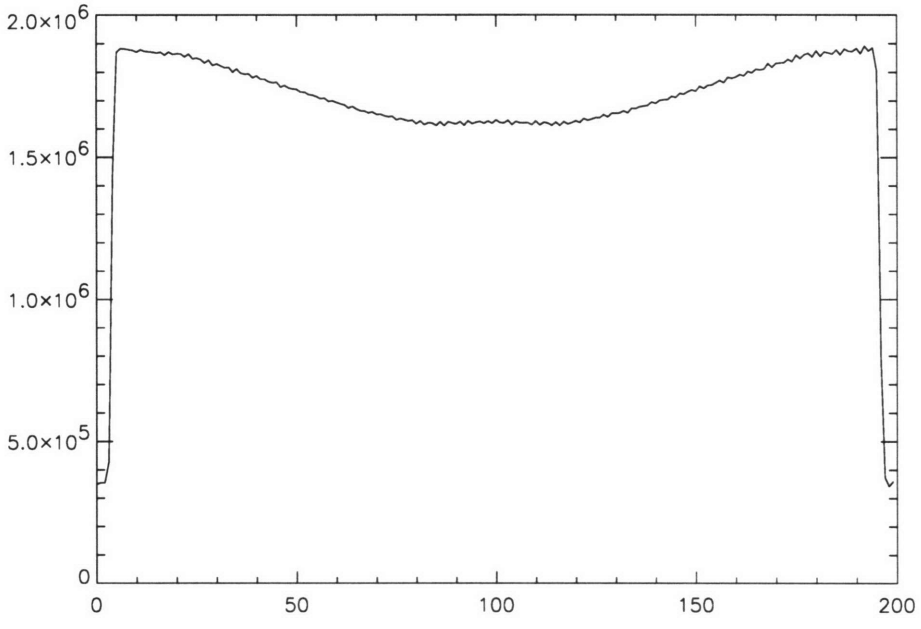

(b)

Figure 5.14 The reconstructed density profile: (a) three-dimensional density profile, (b) the density profile of one projection.

The reconstructed image pixel intensity directly corresponds to the linear attenuation coefficient, which is the product of the mass attenuation coefficient and the material density. However, the mass coefficient is invariant so that the pixel intensity can be normalized with respect to the density profile. From the mushy zone density profile obtained by this CT reconstruction technique, this approach can select a more reliable modeling among the many existing numerical models. The remaining issues for further investigation include noise filtering and smoothing, and point-wise interpolation of the discrete pixel intensity. Furthermore, it will be useful for verifying the mushy zone morphology such as the one shown in Figure 5.15.

Mushy zone morphology affects macro-segregation of compositional species of alloys during casting, because convective transport occurs through pores in the mushy zone. Therefore, knowledge of the mushy zone morphology is essential in estimating convective flow through porous media. Various mushy zone thicknesses will be created in a directionally solidifying mold, as shown in Figure 5.15, using several aluminum alloys such as 2024 and 7075. By comparing the real three-dimensional pictures reconstructed by the proposed sensor with available proposed morphologies in the mushy zone, permeability in the mushy zone will be estimated. In summary, it is confirmed that the proposed CT technique is capable of measuring the continuous distribution of densities from solid to liquid and thus is very useful for alloys which may exhibit a "mushy" solid/liquid interface region.

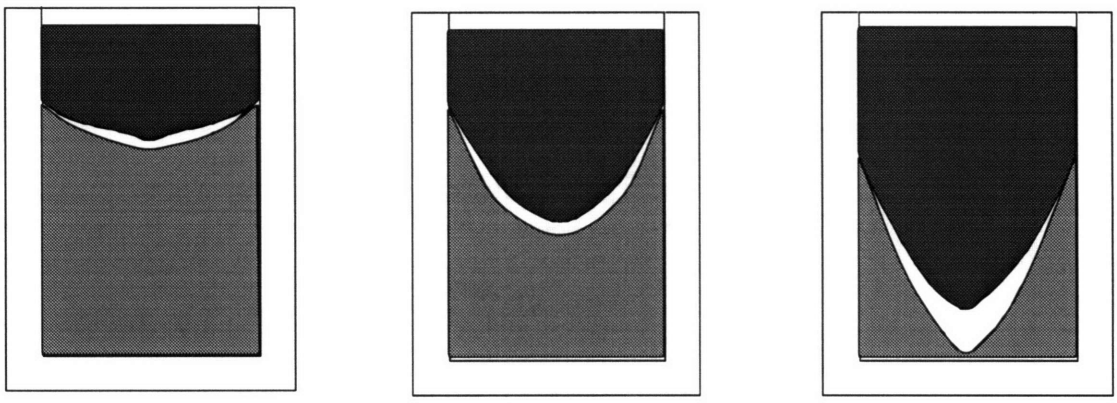

Figure 5.15 Various mushy zone morphologies.

CHAPTER 6

CONCLUSIONS AND FUTURE WORK

6.1 Conclusions

The tomographic sensor developed by the CastScan consortium at MIT for real time monitoring of the solidification front in the continuous casting process accomplishes the two main goals set forth in the project description. Firstly, it provides a new application of industrial computed tomography techniques for non-invasive testing. Furthermore, it can offer tangible economic benefits to the continuous casting industry by preventing break-out incidents and increasing throughput and efficiency by employing optimal process control techniques with the tomographic sensor used as a feedback sensor.

The proposed concept was put into an experimental verification, which proved the viability of this CT sensor and identified the fundamental issues that govern the operation of the sensor. These issues had been individually and collectively analyzed and were addressed in the new sensor design.

The γ-ray sensor integrates numerous system components, including the radiation source, detector array, actuators, and tomographic device. Therefore, in developing an effective sensor that will meet various industrial specifications, effects of each component and their interactions on the overall system must be optimized to achieve the required performance in component design and future system integration.

This thesis proposed a novel non-invasive on-line sensor for detecting the liquid/solid phase interface in the continuous casting process and tested its viability by experimentation. Finally it established design criteria for each system components to meet various performance requirements. In addition, this thesis suggested some useful tomography techniques suitable for detecting the mushy zone.

Chapter 1 discussed the background and motivation for this project. Chapter 2 described the continuous casting processes to augment the understanding of the target application, and how the proposed sensor fits into the overall scheme. In particular, a literature survey on the mushy zone was conducted, since mushy zone dynamics control the quality of the cast metal, and have been a long standing subject of academic speculation. The eventual outcome of this ongoing project will either confirm or modify the current theoretical understanding of the mushy zone.

Chapter 3 investigated some findings and limitations of the CT system observed in the preliminary experiments. These experiments showed that the proposed concept based on radiation attenuation measurements is a viable method for determining the thickness of liquid or solid section of a solidifying metal, with suitable density change resolution of 7% between the liquid and solid phases. In addition, the experiment revealed component requirements for future design, such as the need for a stronger radiation source and a better actuator.

Chapter 4 discussed the required system components comprising the γ-ray sensor and some fundamental issues governing them. In the process, many design choices for equipments and techniques applicable for a wide range of specifications were provided for future reference, and the critical parameters of the CT system were identified and characterized.

Chapter 5 used the design rules set forth in Chapter 4 to design high energy CT sensor components. Through mathematical modeling of the radiation attenuation phenomenon across the liquid and solid interface, clear and quantitative relationships relating source strength and exposure time with other critical system parameters were established. This and other derived forms can serve as a quantitative platform for actual designs. In addition, optimal spatial resolution and tomography techniques for identifying the mushy zone were investigated and confirmed with simulations using the critical parameters as variables. From these steps, the approach of deriving the density profile across the liquid-solid interface from radiation attenuation data and finally generating 3D tomographic image of the density profile offers a superior and more direct method than conventional approaches for geometric identification of the mushy zone.

In conclusion, the tomography system geared for mushy zone identification can serve as a standard model of the proposed sensor. Furthermore, the design guideline developed in the process and laid out in this thesis can be used to derive the future generations of the sensor in different settings and applications.

6.2 Future Work

The future research will involve the development of a full-scale CT system with a high energy x-ray source. A high energy source will enable the data acquisition time to be dramatically speeded up, ideally to a point at which real-time performance is possible. In addition, developing advanced image reconstruction algorithms such as anomaly detection

and the wavelet method for the limited angle reconstruction method should be incorporated not only to solve the hardware restriction but also to increase the performance time.

A larger controlled solidification platform will be designed and fabricated to evaluate the laboratory-scaled designed sensor and to prepare the pilot-scale factory testing. All the design criteria obtained in this thesis will be tested in the MIT lab setting including fan or cone beam detection system, and the shielding requirements to design a optimal prototype design for future different specifications. In addition, the prototype will be installed and pilot testing will be conducted in a commercial industry facility.

REFERENCES

American National Standard, 1993, "For General Radiation Safety: Installation Using Non-Medical X-Ray And Sealed Gamma-Ray Sources", Energies Up To 10 MeV, ANSI N43.3-1993, American National Standards Institute, New York.

Bakken, J.A. and Bergstrom, T., 1986, *Light Metals, 1986*, R.E. Miller, ed., TMS, Warrendale, PA, pp. 883-889.

Beckermann, C. and Wang, C.Y., January 1994, "Incorporating Interfacial Phenomena in Solidification Models, "*Journal of Metals*, pp. 42-47.

Bhatia, M., September 1994, "Wavelet Transform-Based Muti-Resolution Techniques For Tomographic Reconstruction and Detection," Doctoral thesis, Department of Nuclear Engineering, Massachusetts Institute of Technology, Cambridge, MA.

Bobadilla, M., Jolivet, J.M., Lamant, J.Y. and Larrecq, M., 1993, "Continuous Casting of Steel: A Close Connection Between Solidification Studies and Industrial Process Development," *Materials Science and Engineering*, vol. 173, pp. 275-285.

Brooks, R.A. and DiChiro, G., 1976, "Principles of Computer Assisted Tomography (CAT) in Radiographic and Radioisotopic Imaging, *Phys. Med. Bio.*, vol. 21 no. 5, pp. 689-732.

Cember, H., 1992, *Introduction to Health Physics, 2nd edition*, McGraw-Hill, New York.

Chabchoub, F., 1992, "Mathematical Modeling and Experimental Measurements on the Horizontal OHNO Continuous Casting Process," SM Thesis, University of Toronto, Ontario, Canada.

Cho, Z. H., Jones, J. P. and Singh, M., 1993, *Foundations of Medical Imaging*, John Wiley & Sons, New York.

Chu, M.G., 1992, "A Novel Technique for Outlining the Solidification Crater Profile of a Commercial Size Aluminum Alloy Ingot Cast by the Direct Chill Method," *Metallurgical Transactions A*, vol. 23A, pp. 2323-2325.

Chun, J., Lanza, R.C. and Saka, N., April 1994, "Solid/Liquid Interface Detection in Continuous Casting Processes by γ-Ray Attenuation," Massachusetts Institute of Technology, Cambridge, MA, US Patent No. 5,509,460, Serial No. 08/296,342.

Chun, J., Lanza, R. C., Saka, N. and Hytros, M., 1995 "On-Line Monitoring of the Solidification Front in Metal Casting," *Annals of the CIRP*, vol. 44, pp. 181-184.

Copley, D.C., Eberhard, J.W. and Mohr, G.A., January 1994, "Computed Tomography Part 1: Introduction and Industrial Applications," *Journal of Metals*, pp. 14-26.

Dennis, M.J., 1992, "Industrial Computed Tomography, *ASM Handbook, Vol. 17 , Nondestructive Evaluation and Quality Control*, ASM International, Materials Park, OH, pp. 358-386.

Diao, Q.Z. and Tsai, H.L., 1993, "Modeling of Solute Redistribution in the Mushy Zone during Solidification of Aluminum-Copper Alloys," *Metallurgical Transactions A*, pp. 963-972.

Ekenhorst, D., Goebbels, J. and Wolff, V., October 1993, "Application of Microcomputer Tomography for Optimizing the Manufacture of Fiber Ceramics," *Ceramic Forum-International*, pp. 557-560.

Ekens, J.M. and Wagstaff, F.E., 1985, *Light Metals 1987*, R.D. Zabreznik, ed., TMS, Warrendale, PA, pp. 785-791.

Ekens, J.M. and Wagstaff, F.E., 1985, *Light Metals 1985*, H.O. Bohner, ed., TMS-AIME, Warrendale, PA, pp. 1311-1316.

Evans, R. D., 1972, The Atomic Nucleus, 14th edition, McGraw-Hill, New York.

Feldkamp, L.A., Davis, L. C. and Kress, J.W., 1984, "Practical Cone-Beam Algorithm," *J. Optical Society of America,* A, Optics and Image Science, vol. 1, pp. 612-619.

Flemings, M.C., 1974, *Solidification Processing*, McGraw-Hill, New York.

Fossheim, H. and Madsen, E.E., 1979, *Light Metals 1979*, W.S. Peterson, ed., TMS-AIME, Warrendale, PA, pp. 695-720.

Giamei, A.F., January 1993. "Solidification Process Modeling: Status and Barriers," *Journal of Metals*, pp. 51-53.

Glicksman, M.E., Mizenko, L.M., Rettenmayer, M.E. and Marsh, S.P., 1994, "Dendritic Solidification of Undercooled Melts: Mushy Zone Recalescence Dynamics," *Materials Science and Engineering*, vol. 178, pp. 137-146.

Glicksman, M.E., Smith, R.N., Marsh, S.P. and Kuklinski, R., February 1992, "Mushy Zone Modeling with Microstructural Coarsening Kinetics," *Metallurgical Transactions A*, pp. 659-667.

Goldschmit, M.B., Gonzalez, J.C. and Dvorkin, E.N., 1993, "Finite Element Model for Analyzing Liquid Slag Development During Continuous Casting of Round Bars," *Ironmaking and Steelmaking*, vol. 20, no. 5, pp. 379-385.

Huesman, R., Gullberg, G., Greenberg, W. and Budinger, T., 1977, "User's Manual: Donner Algorithms for Reconstruction Tomography," Lawrence Berkeley Laboratory Report No. LBL-214.

Hytros, M., 1996 "A Feasibility Study of Solidification Front Monitoring via Tomographic Imaging," SM Thesis, Department of Mechanical Engineering, Massachusetts Institute of Technology, Cambridge, MA.

Inoue, K., Koezuka, T. and Arita, H., 1990, "Parallel Image Recognition System and Its Application to Steel Making Process," Proceedings of the Sixth International Iron and Steel Congress, Nagoya, Japan, pp. 121-128.

Joseph, P.M. and Spital, R.D., 1978, "A Method for Correcting Bone Induced Artifacts in Computed Tomography Scanners," *J. Comput. Asst. Tomogr.*, vol. 2, no. 2, pp. 100-108.

Jureidini, I., SM Thesis in Progress, Department of Nuclear Engineering, Massachusetts Institute of Technology, Cambridge, MA.

Kalpakjian, S., 1992, *Manufacturing Engineering and Technology, 2nd edition*, Addision-Wesley, Reading, MA.

Knoll, G. F., 1989, *Radiation Detection and Measurement, 2nd edition*, John Wiley & Sons, New York.

Loser, W., Thiem, S. and Jurisch, M., 1993, "Solidification Modeling of Microstructures in Near-Net-Shape Casting of Steels," *Materials Science and Engineering*, vol. 173, pp. 323-326.

McFarland, E.W., "Non-Destructive Evaluation Using Tomography: Physical Principles and Mathematics," University of California at Santa Barbara, CA.

O'Connor, T.G., 1992, "Three-Dimensional Modeling of the Thin Slab Continuous Casting Process," Ph.D. Thesis, University of Illinois at Urbana-Champaign, IL.

Ozgu, M.R., Bright, D.H. and Watkins, D.L., 1985, "Experimental and Mathematical Study of Ingot Solidification, Mold Wall Deflection and Ingot-Mold Interfacial Gap Formation," *Proceedings of the 68th Steelmaking Conference*, Detroit, MI, pp. 315-329.

Pehlke, Robert D., 1992, *ASM Handbook Vol. 15*, Casting ASM International, Materials Park, OH.

Piwonka, T.S., March 1993, "Current Metal Casting Research in the United States," *Foundry International*, p. 4.

Ridder, S.D., Ryes, F.C., Chakravarty, S., Mehrabian, R., Nauman, J.D., Chen, J.H. and Klein, H.J., 1978, *Metallurgical Transactions B*, vol. 9B, pp. 415-425.

Rossi, D.J. and Willsky, A.S., 1984, "Reconstruction from Projections Based on Detection and Estimation of Objects - Parts I and II: Performance Analysis and Robustness Analysis," *IEEE Trans., Acoustics*, ASSP-32, pp. 886-906.

Schonberg Radiation Corporation, 1991, "6 MeV MINAC Operation and Maintenance Manual", Santa Clara, CA.

Shapiro, J., 1972, *Radiation Protection: A Guide for Scientists and Physicians, 3rd Edition*, Harvard University Press, Cambridge, MA.

Shepp, L.A. and Logan, B.F., 1974, "Fourier Reconstruction of a Head Section," *IEEE Trans., Nuc. Sci.*, NS 21:7, p. 21.

Stegemann, D., Reimche, W. and Schmidbauer, J., January 1992, "Investigation of Light Metal Casting Process by Realtime Microfocus Radioscopy," *European Journal of Non-Destructive Testing*, pp. 107-117.

Sugimaru, S., Nakashima, J., Miyazawa, K. and Ogibayashi, S., 1993, "Theoretical Analysis of the Suppression of Solidification Shrinkage Flow in Continuously Cast Steel Blooms," *Materials Science and Engineering*, vol. 173, pp. 305-308.

Teng, Y., 1993, "Finite Element Approaches to Phase Change Problems with Application to Casting Processes," Ph.D. Thesis, Rice University, Houston, TX.